

Article

Geospatial Insights into Ophiolitic Complexes in the Cimmerian Realm of the Afghan Central Block (Middle Afghanistan)

Hemayatullah Ahmadi ^{1,2}, Mohammad Reza Hussaini ², Atal Yousufi ^{2,3,*}, Alma Bekbotayeva ^{3,*}, Akmaral Baisalova ³, Bakytzhan Amralinova ⁴, Indira Mataibayeva ⁵, Abdul Baqi Rahmani ², Emrah Pekkan ⁶ and Naqibullah Sahak ²

¹ Department of Remote Sensing and Geographic Information Systems, Institute of Graduate Programs, Eskişehir Technical University, Eskişehir 26000, Türkiye; h.ahmadi@kpu.edu.af or hahmadi@ogr.eskisehir.edu.tr

² Department of Geological Engineering and Exploration of Mines, Faculty of Geology and Mines, Kabul Polytechnic University, Kabul 1001, Afghanistan; m.reza.h124@gmail.com (M.R.H.); rahmani.baqi58@gmail.com (A.B.R.); dr.sahak.n@gmail.com (N.S.)

³ Department of Geology and Exploration of Mineral Deposits, Institute of Geology and Oil & Gas Engineering, Satbayev University, Almaty 050013, Kazakhstan; a.baisalova@satbayev.university

⁴ Institute of Project Management, Satbayev University, Almaty 050013, Kazakhstan; b.amralinova@satbayev.university

⁵ School of Earth Sciences, D. Serikbayev East Kazakhstan Technical University, Ust-Kamenogorsk 70004, Kazakhstan; indiramataibayeva@gmail.com

⁶ Institute of Earth and Space Sciences, Eskişehir Technical University, Eskişehir 26000, Türkiye; epekkkan@eskisehir.edu.tr

* Correspondence: a.yousufi@stud.satbayev.university or a.yousufi@kpu.edu.af (A.Y.); a.bekbotayeva@satbayev.university (A.B.)



Citation: Ahmadi, H.; Hussaini, M.R.; Yousufi, A.; Bekbotayeva, A.; Baisalova, A.; Amralinova, B.; Mataibayeva, I.; Rahmani, A.B.; Pekkan, E.; Sahak, N. Geospatial Insights into Ophiolitic Complexes in the Cimmerian Realm of the Afghan Central Block (Middle Afghanistan). *Minerals* **2023**, *13*, 1453. <https://doi.org/10.3390/min13111453>

Academic Editor: Basilios Tsikouras

Received: 24 August 2023

Revised: 8 November 2023

Accepted: 12 November 2023

Published: 18 November 2023



Copyright: © 2023 by the authors. Licensee MDPI, Basel, Switzerland. This article is an open access article distributed under the terms and conditions of the Creative Commons Attribution (CC BY) license (<https://creativecommons.org/licenses/by/4.0/>).

Abstract: Ophiolites are remnants of oceanic crust that have been thrust onto continental crust due to tectonic processes. They are composed of mostly mafic and ultramafic rocks, which are genetically associated with gold, silver, platinum group element (PGE), chrome, manganese, titanium, cobalt, copper, and nickel deposits. The main objective of this research was to identify the spatial distribution of Mesozoic ophiolitic complexes within the Central Afghan Block in Middle Afghanistan using optical remote sensing data and spectral analyses. Distinct algorithms, such as false color composite (FCC), proposed band ratios (PBR), principal component analysis (PCA), and spectral angle mapper (SAM), were used to map the targeted ophiolitic complexes. New band ratios were proposed in this study based on the spectral properties of mafic-ultramafic minerals and rocks, which showed high efficiency. Based on the results, four different ophiolitic complexes were delineated within this study area. These complexes are consistent with previous studies. The accuracy assessment of this study showed an overall accuracy of 72.2%. The findings of this study can significantly contribute to further studies on the emplacement mechanism and paleo-Tethys history of Middle Afghanistan. Also, the spatial distribution of the ophiolitic complexes identified in this study can be used to constrain models of the tectonic evolution of the Central Afghan Block. Additionally, the identification of new band ratios for mapping ophiolitic complexes can be used in future studies of other ophiolite-bearing regions.

Keywords: ophiolites; Cimmerian realm; middle Afghanistan; remote sensing; ASTER

1. Introduction

Ophiolites are sections of oceanic crust and upper mantle that have been uplifted and exposed on land. They are valuable natural laboratories for studying the formation and evolution of the oceanic crust, and have been classified into many groups based

on their composition and tectonic setting [1–3]. According to a recent definition by [4], ophiolites are fragments of the oceanic lithosphere that formed at mid-ocean ridges, back arc basins, or forearcs. They are characterized by a specific sequence of rocks, including pillow basalts, layered gabbros, sheeted mafic dykes, depleted ultramafic rocks, podiform chromite, pelagic sediments, and plagiogranite. Although ophiolites may be structurally displaced and sometimes lack sheeted dykes and gabbros, most investigators agree that they must contain some combination of tholeiitic pillow basalts, gabbros, and related depleted ultramafic rocks [1,5].

The types and classification of ophiolites are determined by two main factors: tectonic setting and displacement mechanism [2,6]. Dilek and Furnes (2011) classified ophiolites into five tectonic settings based on their geochemistry and petrogenesis, and these ophiolites are distributed globally: Continental margin (Ex. Ligurian and Western Alpine ophiolite, Jormua, Finland), mid-ocean ridge (Ex. Macquarie Ridge, Masirah, Oman, or Taitao, Chile), plume type (Ex. Nicoya in Costa Rica or Bolivar in Colombia), suprasubduction type (Ex. Troodos in Cyprus, Kizildag in Turkiye, Semail in Oman, or Betts Cove in Canada), and volcanic arc type (Ex. Rocas Verdes in Chile or Solund-Stavfjord in Norway) [1]. According to the recent definition of ophiolites by [4], only mid-ocean ridge and supra-subduction ophiolites are considered to be true ophiolites.

The distribution of ophiolites in Afghanistan is a reflection of its geological development. The accretion of Gondwana-derived fragments to the active margin of Laurasia since the end of the Paleozoic is evident in the emplacement of ophiolites along distinct suture zones [2,7]. Three large-scale ophiolite complexes are found in Afghanistan: the Khost, Kabul, and Panjao complexes. However, some other smaller fragments of ophiolites are also found in the central and northeastern parts of the country [2,3,7,8]. The distribution of ophiolites in Afghanistan is associated with the Alpine and Cimmerian orogenic events along suture zones, as well as the closure of the Paleo-Tethys Ocean during the Jurassic and Cretaceous periods [3,9,10]. According to [7], two suture zones are present in central Afghanistan: the Herat and Panjao suture zones. Two other suture zones, the Kabul and Khost suture zones, are separated from these two in eastern Afghanistan.

Ophiolites have been studied from a variety of perspectives worldwide. Conventional studies of ophiolites have focused on their geochemistry, mineralogy, petrology, and emplacement mechanisms, primarily in suture zones. However, technological advances have enabled the use of remote sensing to study the spatial distribution of ophiolite complexes. Recently, geoscientists have used geospatial technology to study the distribution of ophiolite complexes for their effectiveness, cost-efficiency, and time savings. This has allowed them to better understand the emplacement mechanism of ophiolites.

Varieties of multispectral remote sensing data can be used to map ophiolite complexes and their associated altered rocks and minerals, such as the Advanced Spaceborne Thermal Emission and Reflection Radiometer (ASTER) [3,11–13], Sentinel-2MSI [14,15], Landsat-8 OLI/TIRS [16–19], and hyperspectral data [20–22].

A wide range of spectral analysis algorithms have been used with different remote sensing data to identify ophiolite complexes in various parts of the world, particularly in arid and semi-arid regions. For instance, false color composite (FCC), band ratio (BR), spectral index (SI) [2,3,23–26], minimum noise fraction (MNF), principal component analysis (PCA), spectral feature fitting (SFF) [16,27–31], spectral angle mapper (SAM), relative absorption band depth (RBD), support vector machine (SVM), random forest classification (RFC) [3,32–35], machine and deep learning [36–39] have been used.

Past investigations of ophiolites in Afghanistan are limited. Previous studies have focused on the Logar ophiolitic complex in the Kabul Block and its relationship to chromite ore [2,3,8,40]. These studies have mapped the spatial distribution of mafic-ultramafic rocks and minerals and their associated altered bodies within the Logar region. The most recent study by Yousufi et al. (2023) integrated remote sensing geological data to study the mineralogical and petrographic properties of dunite peridotite, serpentinite, and other alteration minerals in Logar, southeastern Afghanistan. The central Afghanistan ophiolite,

linked to the Cimmerian orogeny, is of considerable scientific importance. Investigating their spatial distribution, tectonic contexts, and connections to industrial minerals is crucial. Despite this significance, only a few recent studies have been undertaken in this region. Traditional exploration of ophiolitic complexes in central Afghanistan demands substantial financial resources and extensive fieldwork, which can be time-intensive and currently less feasible. Consequently, an optimal strategy involves harnessing remote sensing technology to map out the spatial extent of the ophiolitic complex and its associated alteration minerals. Given the present constraints, this approach offers an efficient and cost-effective alternative.

Henceforth, the principal objectives of this study encompass: (1) to conduct an in-depth remote sensing analysis aimed at precisely delineating the spatial distribution of Mesozoic ophiolitic formations situated in central Afghanistan using ASTER data; (2) to empirically evaluate the effectiveness of spectral analysis by subjecting the obtained results to rigorous verification procedures; and (3) to innovate and propose new band ratios tailored to discern mafic-ultramafic bodies based on their distinctive spectral attributes.

The findings of this study will make a significant contribution to the past and present tectonic studies of the region. This study can pave the way for detailed investigations of the emplacement mechanisms of ophiolites in Afghanistan. In addition, the methodology applied in this study will provide valuable insights into remote sensing studies and can be replicated in other arid and semi-arid regions of the world.

2. Geologic and Tectonic Settings of the Study Area

This study area is located in the central highlands of Afghanistan, between latitudes $34^{\circ}00'00''$ N and $34^{\circ}30'00''$ N, and longitudes $66^{\circ}30'00''$ E and $68^{\circ}00'00''$ E. It covers the Panjab and Waras districts of Bamyan province and the Makazi Behsud district of Maidan Wardak province (Figure 1). The area is mountainous and steep, with an altitude ranging from 2012 to 4200 m. The main river crossing the area is the Helmand River. The climate is semi-arid, with a very snowy winter and a gentle spring and summer [41].

Afghanistan and the surrounding areas are a mosaic of continental blocks separated by complex faults. These faults have been active until very recently, as evidenced by the recent earthquakes in the region. Some of the faults are east - west, running parallel to the major regional structures. Others are transversal, cutting across the regional structures [42,43]. Afghanistan and surrounding regions present a mosaic of continental blocks originating from Gondwanaland [42,44]. The Hercynian orogeny belt, characterized by subduction-related events, has an extensive presence in Afghanistan, along with a few scattered rock exposures in the northern parts of Iran. This orogenic belt was formed along the boundary between the Paleo-Tethys oceanic region and the Turan-Turkestan-Tarim blocks. The northern Eocimmerian orogenic belt is a collision-type orogen widely represented in Afghanistan and the north of Iran. It was formed due to the closure of the Paleo-Tethys Ocean and the collision of the Central Iran and Central Afghanistan blocks with the Turan-Turkestan-Tarim block. The southern Eocimmerian orogenic belt may be present beneath the Neogene and Quaternary formations of southern Afghanistan. The orogen was constructed at the margin between the Neo-Tethys and the central Iran-central Afghanistan block, which was itself subjected to regional extension at that time. The belt is now incorporated into the Alpine-Himalayan orogen [9,42,44].

Central Afghanistan (the study area) was part of Gondwana in the Paleozoic. It was overlain by Cambrian to Permian–Triassic sediments with no Paleozoic orogeny. In contrast to regions to the east of the Chaman fault, the strongest tangential tectonics in central Afghanistan occurred in the middle of the Mesozoic [41,45]. The Panjao suture, a major geological feature in central Afghanistan, crosses the regions of Panjao (Panjab) and Waras. It trends southwest for 500 km. A thick sequence of upper Triassic to Jurassic flysch and ophiolitic melanges composed of exotic blocks of Permo–Triassic limestones has been observed within the extent of this suture zone (Figure 2) [42]. The mélanges are difficult to study because they are now in steeply dipping slices. However, the ophiolites are likely remnants of oceanic crust that was thrust over the region in the Upper Jurassic/Lower

Cretaceous. This is because the Barremian and Aptian epicontinental sediments lie on top of the mélanges. The discovery of glaucophane in some amphibolites suggests that high-pressure metamorphism also occurred in this belt [42,44,46–49].

According to [7,50], tertiary tectonics in central Afghanistan appear to have been dominated by strike-slip faulting. This is evident in the vertical slices of sediment of various ages along a number of major faults, whose strikes vary from northeast close to the Chaman fault to east-west close to the Herat fault (Figure 2).

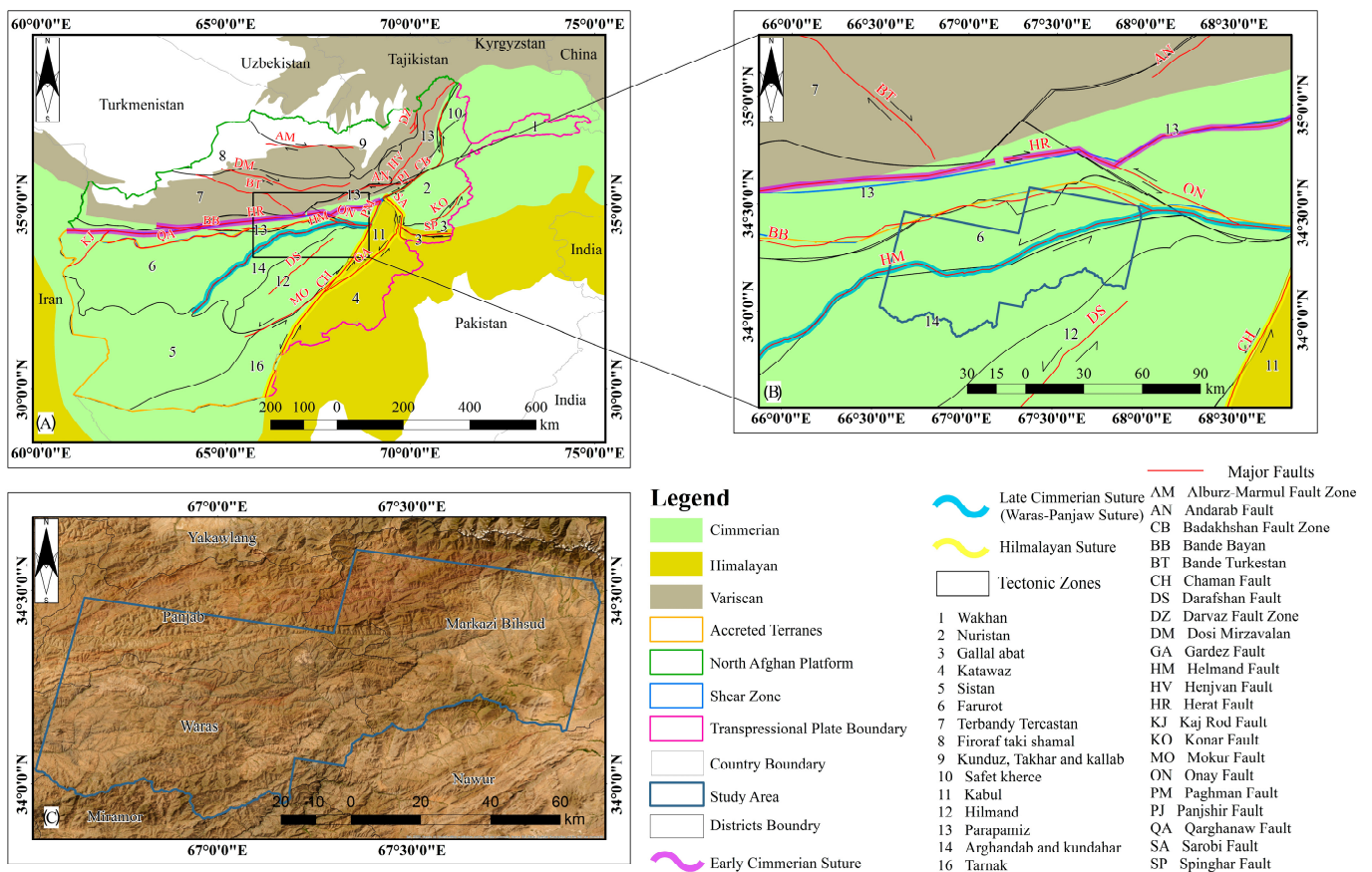


Figure 1. Geographic and tectonic sketches of study area in central Afghanistan; (A) extend of study area within the orogenic belts, local tectonic zones, and major active faults of Afghanistan modified from [9,41–44,48–50]; (B) tectonic location of study area within the extend of Cimmerian orogenic belt in central Afghanistan; (C) geographical and geomorphological settings of study area and surrounding regions compiled from ArcMap basemaps.

According to [41], distinct formations of metamorphic and igneous rocks of Proterozoic, Paleozoic, Mesozoic, and Cenozoic ages can be observed within this study area (see Figure 2). Proterozoic formations, consisting of quartzite, amphibolite, marble, and schist of varying thicknesses, are prevalent across the southern regions of the Marki Behsud and Waras districts. The basement rocks exhibit distinct contacts with Paleozoic and Mesozoic formations due to the presence of the strike-slip Helmand fault (refer to Figure 2). Paleozoic formations, encompassing Carboniferous–Permian and Permian-aged sediments, are found to restricted extents within the southeast and northeast regions of the Marki Behdsud district. These formations consist of marble, sandstone, schist, siltstone, and mafic volcanic rocks, as depicted in Figure 2. On the other hand, Mesozoic sediments, comprising Triassic, Jurassic, and Cretaceous rocks, exhibit a widespread distribution within the northern portions of this study area. These sediments are primarily composed of siltstone, conglomerate, shale, limestone, and fragments of acidic and mafic volcanic rocks, as illustrated in Figure 2. The Cenozoic sedimentary cover, encompassing Paleogene,

Neogene, and Quaternary-aged deposits, exhibits distinct distribution patterns within both the northern and southern regions (Figure 2).

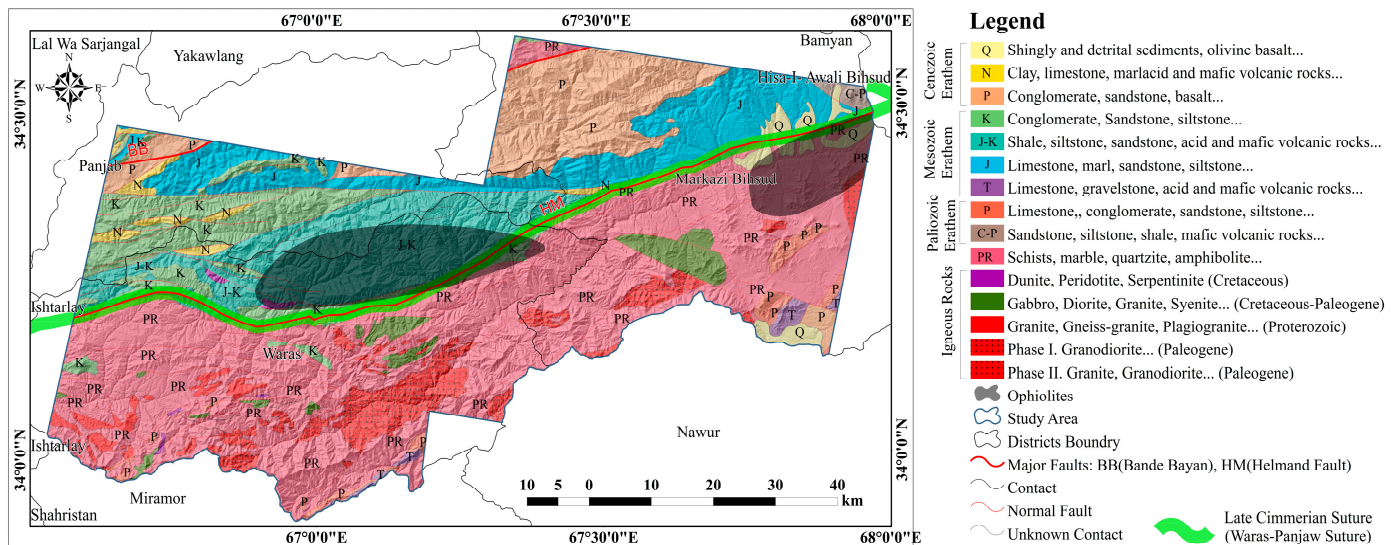


Figure 2. Simplified geological map study area covering Marki Behsud and Panjab districts over central Afghanistan, modified from [7,9,41].

Magmatic activity is concomitant with a series of acid, mafic, and ultramafic complexes, predominantly situated across the southern and central sectors of this study area. Notably, ultramafic lithologies such as dunite peridotite, and serpentinite, of probable Cretaceous age, are present as lens-like bodies within the central and southwestern zones, often aligning with fault zones (Figure 2). Gabbro, diorite, as mafic rock formations, are prominently associated with the occurrence of ultramafic lenses across numerous sectors, primarily constituting the ophiolitic complex within this region. In addition, phase-I granite, granodiorite, and gneissic granites, all of Paleogene age, have intruded into the Proterozoic formations within the southern reaches of this study area (refer to Figure 2) [7,41].

3. Materials and Methods

This study was meticulously assembled through an extensive remote sensing analysis, complemented by subsequent fieldwork to validate the obtained results. A diverse array of academic resources, including journal articles, conference proceedings, books, published geological reports, maps, and authoritative official websites, were diligently reviewed to conduct an in-depth literature review and thorough background research. As depicted in (Figure 3), the remote sensing studies in this work encompass pre-processing, processing, and post-processing stages. The utilization of Advanced Spaceborne Thermal Emission and Reflection Radiometer (ASTER) data facilitated the mapping of ophiolitic complexes along with their associated alteration minerals and rocks. The raw data underwent a preprocessing stage for radiometric calibration and atmospheric corrections prior to object extraction. Finally, the extracted objects underwent post-processing for validation as well as to elucidate their geological and tectonic implications.

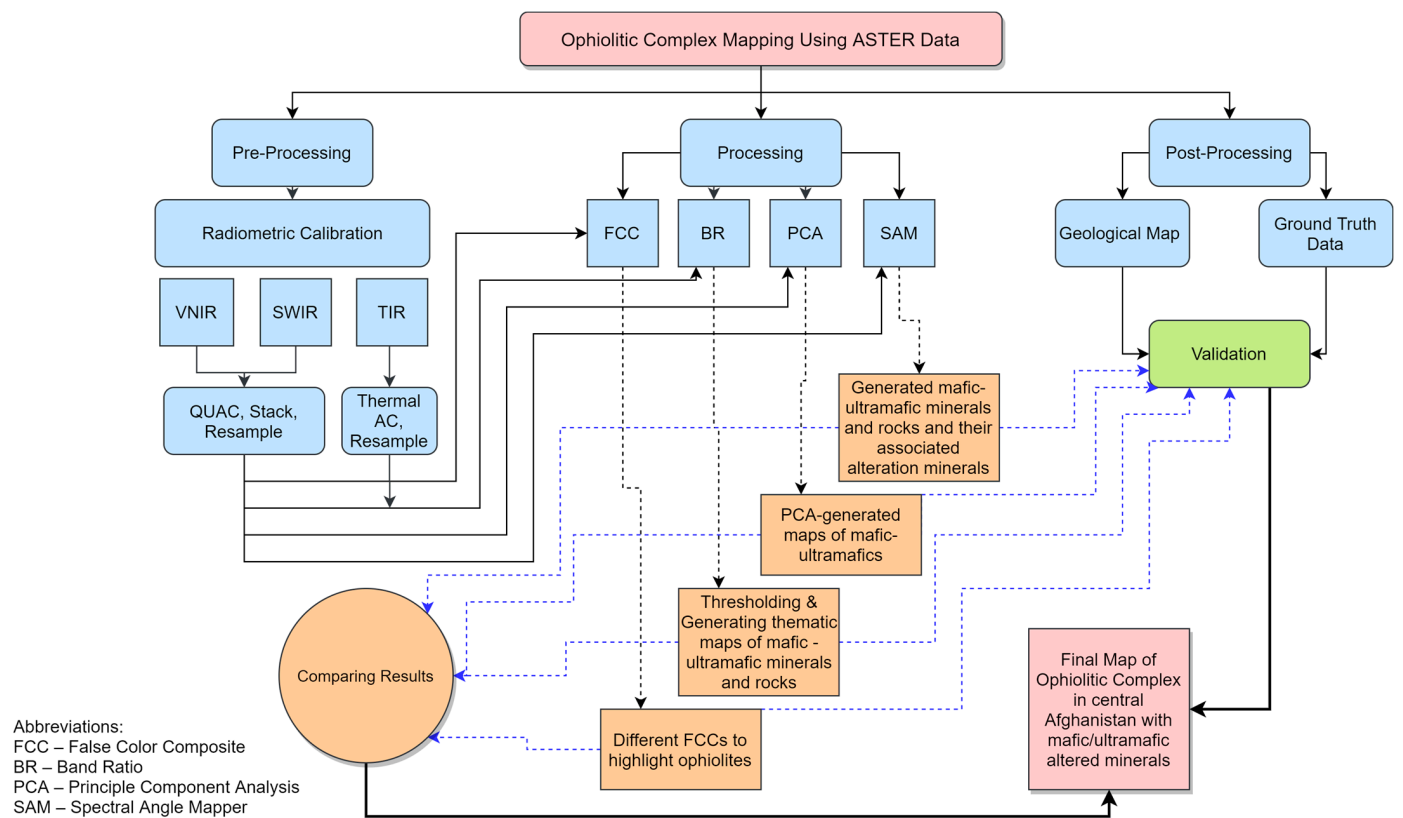


Figure 3. Methodology flowchart for this study.

ASTER, a collection of multispectral imageries, was launched aboard NASA's Terra platform within the Earth Observing System (EOS) in December 1999 [3,50,51]. The detailed specifics of the ASTER data are elucidated in (Table 1).

Table 1. Description of ASTER data based on [3,52].

Subsystems	Band No	Spectral Range (µm)	Spatial Resolution (m)	Radiometric Resolution
VNIR	1	0.52–0.60	15	8 bits
	2	0.63–0.69		
	3N	0.78–0.86		
	3B	0.78–0.86		
	4	1.60–1.70		
SWIR	5	2.145–2.185	30	8 bits
	6	2.185–2.225		
	7	2.235–2.285		
	8	2.295–2.365		
	9	2.360–2.430		
	10	8.125–8.475		
TIR	11	8.475–8.825	90	12 bits
	12	8.925–9.275		
	13	10.25–10.95		
	14	10.95–11.65		

For this study, two distinct tiles of ASTER data covering the entire study area were acquired from NASA's official website (Earthexplorer). The time frame chosen for downloading falls within the summer season, when atmospheric precipitation is at its lowest. A condensed overview of the tile descriptions can be found in Table 2.

Table 2. Specifications of the downloaded ASTER data extend to cover this study area.

No	Tile ID	Latitude	Longitude	Acquisition Date
1	AST_L1T_00308252001062523_20150419005002_30352	34.29369	67.58912	25 August 2001
2	AST_L1T_00308192002062551_20150424123453_18609	34.17228	66.90345	19 August 2001

In addition to the remote sensing data, a geological map of Afghanistan with a scale of 1:500,000 was also utilized to verify and establish the relationship between the remote sensing findings and the geological context of this study area.

To facilitate processing, a variety of spectral analyses were employed on the ASTER data. These included techniques such as false color composite (FCC), band ratio (BR), principal component analysis (PCA), and spectral angle mapper (SAM). These methodologies were used to map the spatial distribution of mafic-ultramafic rocks (ophiolites) and their associated alteration minerals. The ultimate outcomes were validated through ground-truth data collected during fieldwork and observations conducted across this study area. During the fieldwork, we made efforts to gather GPS data points from the mafic-ultramafic exposures in order to validate the accuracy of the obtained results. Additionally, we conducted macroscopic examinations of the collected samples to assess their physical characteristics and overall observations. ENVI 5.3, QGIS 3.34, and Google Earth Pro software v.7.3.6 were employed for satellite imagery processing, analysis, and interpretation. Meanwhile, ArcMap 10.5 was utilized for plotting and other vectorial processing tasks.

3.1. False Color Composite

False color composite is a method of enhancing color composites that involves arranging three distinct multispectral or thermal bands in a sequence of red, green, and blue channels [51]. When the arranged bands consist of red, green, and blue, the amalgamation is termed a true-color combination, displaying the object in its genuine hues. Conversely, a false-color combination arises when alternate channels of the electromagnetic spectrum replace the RGB bands, resulting in an image of the object that does not present its innate colors [53].

Various configurations of false color composites (FCCs) are employed across the visible-near infrared (VNIR), shortwave infrared (SWIR), and thermal infrared (TIR) bands in ASTER data. This approach aids in displaying potential zones containing distinct rock types and minerals [40,54]. Drawing from the studies conducted by [13,55], this research explored three distinct false color composites (FCCs): 463, 432, and 193, each serving as RGB channels. The results of these combinations are discussed further. The first two combinations yielded the best results, primarily attributed to the higher reflectance of ultramafics within the VNIR-SWIR spectral range (Figures 4 and 5).

3.2. Band Ratio

Band rationing and spectral indexing are techniques that enhance the spectral differences between two bands of a multispectral image by dividing the values in one band by the values in another band. This is conducted based on the spectral characteristics of the objects that are being imaged [2,3,53,56]. BR is calculated using the below formula:

$$BV_{I,j,r} = \frac{I}{BI_{i,j,l}} \quad (1)$$

In this context, $BV_{i,j}$, and r represent the pixel output at the intersection of r th i and column j . Similarly, $BV_{i,j}$, and k denote the brightness value in band k at that specific position, while $BV_{i,j}$, and l indicate the brightness value in band l [51].

Band ratio is considered one of the most useful and significant techniques for the extraction of information and is also widely used for lithological mapping of different geological units [51,57–62]. The ratios stem from the crests and troughs of reflectance curves.

Typically, this involves dividing the band characterized by high reflectance by the one with low reflectance. This approach enhances specific attributes or substances that might remain hidden in the initial spectral bands. Moreover, it mitigates issues like shadows and terrain-related distortions, rendering it well-suited for intricate landscapes [51,60]. Based on [3,61], the primary minerals found in mafic rocks include plagioclase, olivine, and pyroxene. These minerals are susceptible to alteration, giving rise to chlorite, epidote, calcite, iron oxides, and hydroxides. On the other hand, ultramafic rocks predominantly comprise pyroxene and olivine. These minerals, when subjected to alteration, transform into the serpentine group, primarily consisting of antigorite and chrysotile, along with smaller quantities of brucite and talc. These transformations are a result of hydrothermal alteration processes.

Utilizing the spectral attributes of mafic-ultramafic rocks and their alteration minerals, the prevailing band ratios commonly referenced in the literature for ASTER data encompass: 5/7, 4/5, 3/1, 4/7, 4/1, 3/5, 7/6, 3/4 [16,34,58,59].

In this study, primarily three band ratios were employed: 12/14 to identify mafic-ultramafic bodies, and 4/6 and 4/8 to delineate carbonate formations. [3,61]. Furthermore, based on the diagnostic spectral attributes and distinctive characteristics of mafic-ultramafic rocks, which are between 0.556 and 2.4 μm , minerals, and their altered compositions as illustrated in Figures 4 and 5 (sourced from [62]) and the USGS spectral library, novel band ratios have been introduced. These ratios are listed in Table 3 for easy reference.

Table 3. Proposed ASTER band ratios for ophiolitic rocks and associated alteration minerals in this study.

Satellites/Sensor	Proposed Band Ratio	Ophiolitic Rocks/Minerals
ASTER	4/3	Dunite Peridotite
	2/6	Pyroxenite
	1/9	Peridotite, Basalt
	4/9	Gabbro
	3/8	Gabbro, Basalt
	3/9	Gabbro, Basalt
	5/3	Chlorite
	4/8	Serpentine, Talc + Calcite
	5/1	Epidote, Dolomite

3.3. Principal Component Analysis

Principal component analysis (PCA) is a statistical technique that can be used to transform a set of correlated variables into a set of uncorrelated variables [53]. This is conducted by finding a new set of variables, called principal components, that are linear combinations of the original variables. The principal components are ordered by their variance, so the first principal component will have the highest variance, the second principal component will have the second highest variance, and so on [16,29,63]. In the context of image data, PCA can be used to reduce the dimensionality of the data while preserving as much of the information as possible. This is conducted by finding a small number of principal components that capture most of the variance in the original data. The resulting images will be composed of a smaller number of bands, but each band will contain more distinct information than a band in the original image [35,53].

PCA techniques are widely used for lithological mapping, as well as for detecting alteration and mineralization zones. In this context, the ASTER VNIR and SWIR bands hold particular significance due to their high degree of correlation [29]. In this study, we employed the PCA approach to identify mafic-ultramafic rocks, such as dunite peridotite, gabbro, and basalt, which constitute the ophiolitic complex. Additionally, we discerned

minerals like chlorite, talc, calcite, dolomite, and epidote, indicative of mafic-ultramafic alteration minerals, through the same PCA technique.

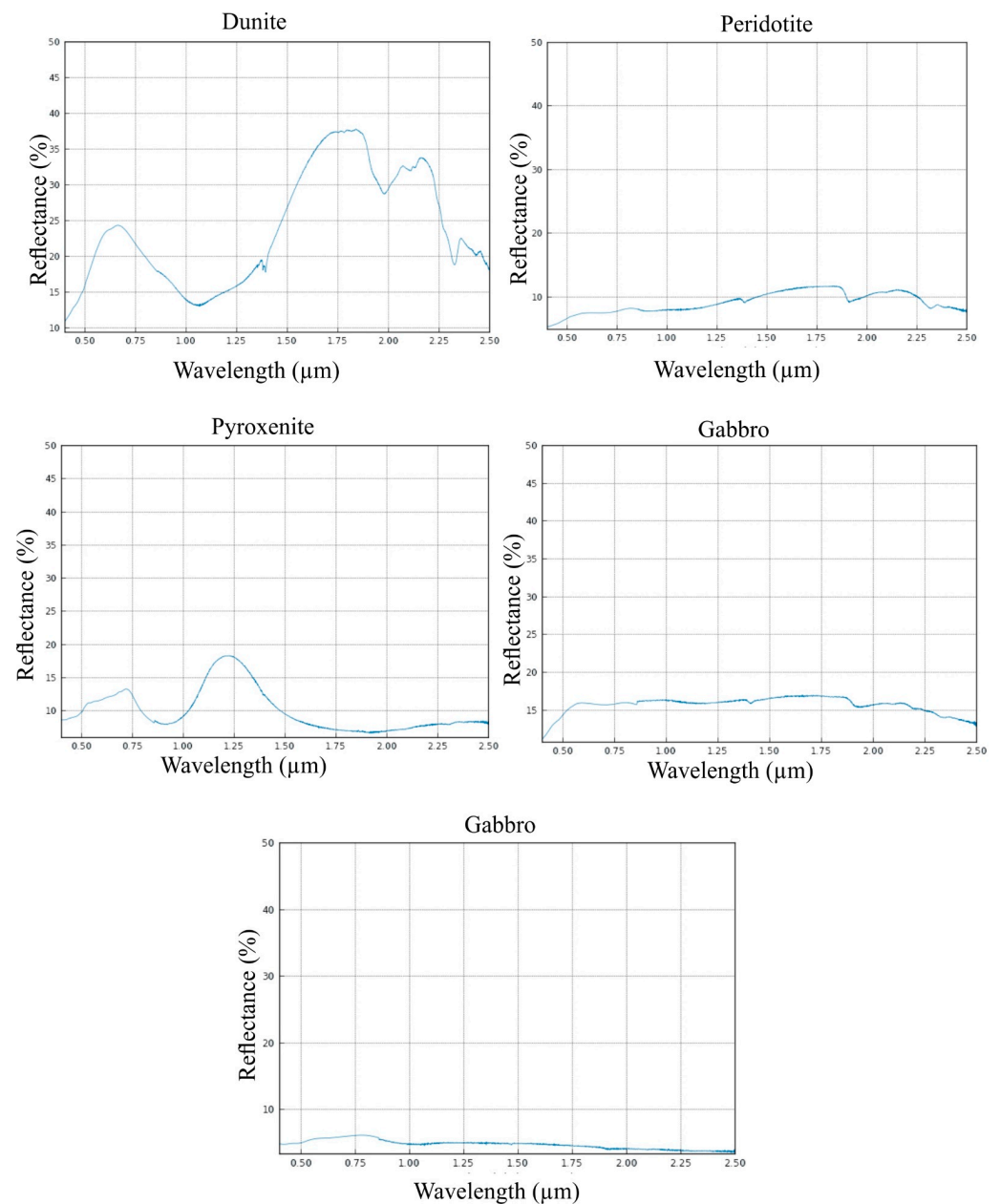


Figure 4. Spectral signature of mafic-ultramafic rocks within the range of (0.50–2.50 μm) modified from [62].

Taking into account the spectral signatures of these rocks and minerals (Figures 4 and 5), the analysis primarily focused on the multispectral bands (VNIR + SWIR) of ASTER data. The bands chosen for the analysis were determined by considering the peaks and troughs of reflection and absorption associated with the specific rocks and minerals under investigation (Figures 4 and 5). Following the PCA analysis, the most promising principal component (PC) was chosen by identifying two bands with values of opposite signs and significant differences in eigenvectors, as detailed in (Tables 4 and 5). Recognizing that mosaicking multiple tiles can occasionally lead to issues during statistical analysis, PCA was independently performed on each individual tile. Subsequently, the results were amalgamated into unified maps, a topic that will be further elaborated upon.

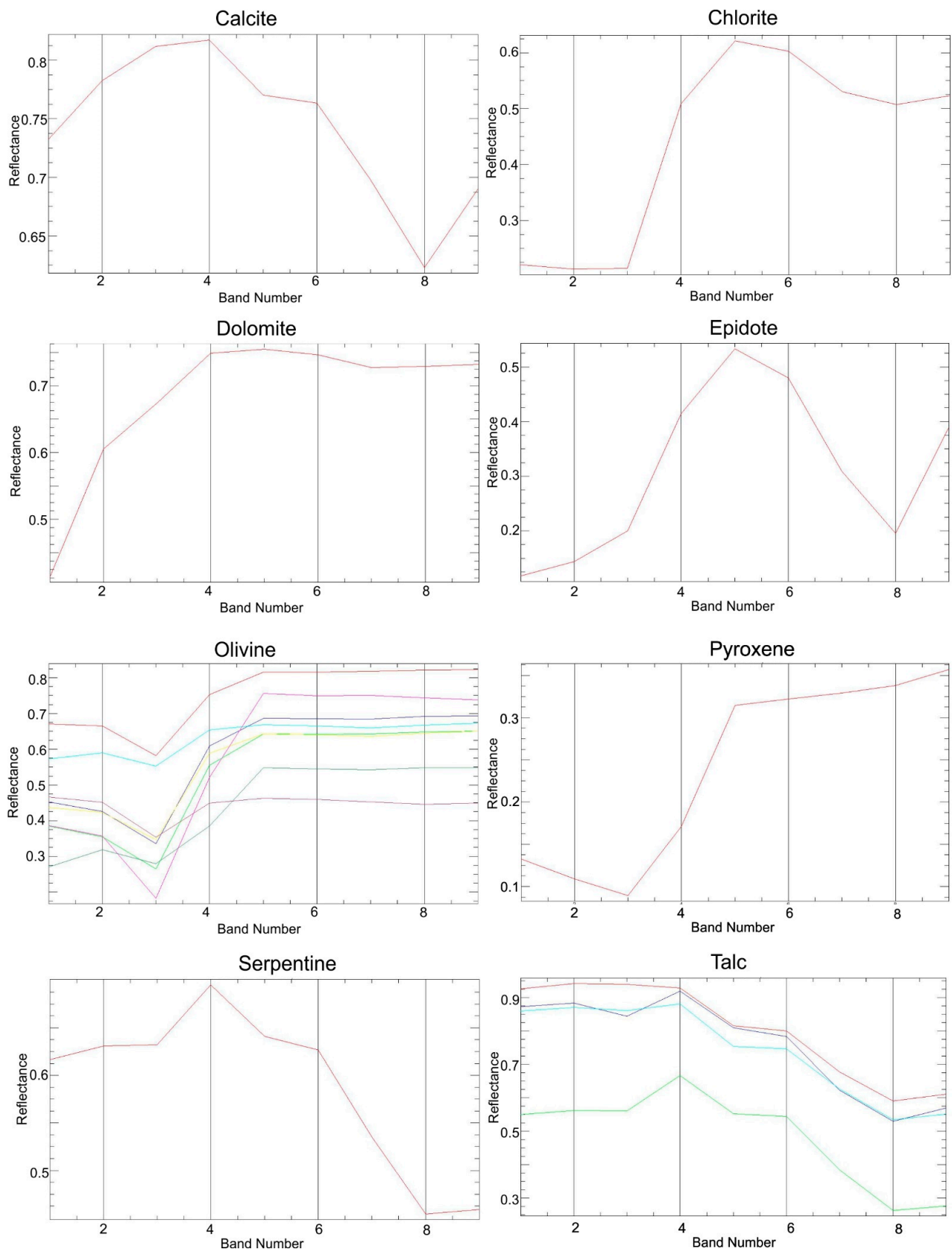


Figure 5. Spectral signature of mafic-ultramafic primary and alteration minerals reproduced and resampled from the USGS spectral library.

Table 4. PCA analysis of multispectral ASTER data for mafic-ultramafic rock detection.

Tile No 1						Tile No 2					
Dunite											
Eigenvector	Band 1	Band 3	Band 4	Band 6	Eigenvalue	Eigenvector	Band 1	Band 3	Band 4	Band 6	Eigenvalue
PC1	0.987076	−0.11292	−0.092764	0.065771	0.090936	PC1	0.991175	−0.00972	−0.130986	−0.0179	0.076236
PC2	−0.10632	−0.98095	0.131024	0.096302	0.004027	PC2	0.004224	−0.9731	0.130159	−0.19004	0.001328
PC3	−0.07328	0.079341	−0.183588	0.977052	0.00054	PC3	−0.12961	−0.14414	−0.978894	0.064743	0.000577
PC4	0.094908	0.136748	0.969806	0.17824	0.000429	PC4	0.027503	−0.17946	0.087565	0.979475	0.000312
Pyroxenite											
Eigenvector	Band 1	Band 2	Band 4	Band 6	Eigenvalue	Eigenvector	Band 1	Band 2	Band 4	Band 6	Eigenvalue
PC1	0.986174	−0.1374	0.067083	−0.0639	0.087974	PC1	0.994808	−0.05014	−0.087554	0.013348	0.067865
PC2	−0.13781	−0.98181	0.097656	0.086744	0.003858	PC2	−0.05908	−0.99041	−0.112475	−0.05435	0.001479
PC3	−0.05424	0.104619	0.992835	−0.01977	0.000538	PC3	0.080826	−0.11837	0.989439	0.021587	0.000364
PC4	−0.07434	−0.07893	−0.015539	−0.99398	0.000096	PC4	−0.01827	−0.05069	−0.02635	0.9982	0.000063
Peridotite											
Eigenvector	Band 1	Band 2	Band 8	Band 9	Eigenvalue	Eigenvector	Band 1	Band 2	Band 8	Band 9	Eigenvalue
PC1	0.986174	−0.1374	0.067083	−0.063896	0.087974	PC1	0.99283	−0.0772	−0.084745	−0.033879	0.072021
PC2	−0.13781	−0.98181	0.097656	0.086744	0.003858	PC2	−0.08549	−0.98909	−0.114647	0.035288	0.001096
PC3	−0.05424	0.104619	0.992835	−0.019772	0.000538	PC3	0.075817	−0.12051	0.989589	0.021059	0.000161
PC4	−0.07434	−0.07893	−0.015539	−0.993983	0.000096	PC4	0.035106	0.034875	−0.019693	0.998581	0.000074
Gabbro											
Eigenvector	Band 3	Band 4	Band 8	Band 9	Eigenvalue	Eigenvector	Band 3	Band 4	Band 8	Band 9	Eigenvalue
PC1	0.997215	0.050312	−0.0289	0.046858	0.079917	PC1	0.994491	−0.07535	0.067791	−0.02673	0.097971
PC2	0.04867	−0.99699	0.029369	0.052814	0.004159	PC2	−0.06607	−0.9863	−0.14451	−0.04432	0.00141
PC3	0.027295	0.030883	0.999148	0.00222	0.000385	PC3	−0.07847	−0.13813	0.986931	−0.02702	0.000439
PC4	0.049482	−0.05036	0.002421	−0.9975	0.000127	PC4	0.02157	−0.04955	0.022113	0.998294	0.00017
Basalt											
Eigenvector	Band 2	Band 3	Band 8	Band 9	Eigenvalue	Eigenvector	Band 2	Band 3	Band 8	Band 9	Eigenvalue
PC1	0.994922	0.096247	−0.02824	0.00835	0.074576	PC1	0.993671	0.002424	0.072208	−0.08601	0.083341
PC2	0.097048	−0.99475	0.031275	0.008354	0.003522	PC2	−0.00595	0.977309	0.180629	0.110479	0.001016
PC3	0.025072	0.033864	0.999112	0.000685	0.000384	PC3	0.073712	0.177945	−0.98071	0.033271	0.000435
PC4	−0.00914	0.007483	−0.00071	0.99993	0.000124	PC4	0.084554	−0.11488	0.019083	0.98959	0.000157

Table 5. PCA analysis of multispectral ASTER data for mafic-ultramafic mineral detection.

Tile No 1						Tile No 2					
Chlorite											
Eigenvector	Band 2	Band 3	Band 5	Band 6	Eigenvalue	Eigenvector	Band 2	Band 3	Band 5	Band 6	Eigenvalue
PC1	0.999625	−0.00197	−0.02669	0.005867	0.088405	PC1	0.993617	0.081199	0.077181	−0.013216	0.072439
PC2	−0.00113	−0.99945	0.032608	0.005671	0.00374	PC2	0.090669	−0.986679	−0.133124	−0.022822	0.001337
PC3	0.026752	0.032554	0.999109	−0.00222	0.000382	PC3	−0.065411	−0.139255	0.988089	−0.003012	0.000439
PC4	−0.0058	0.005752	0.002186	0.999964	0.000165	PC4	0.015009	−0.021872	0.000958	0.999648	0.000113
Serpentine											
Eigenvector	Band 4	Band 5	Band 8	Band 9	Eigenvalue	Eigenvector	Band 4	Band 5	Band 8	Band 9	Eigenvalue
PC1	0.98688	0.157311	−0.03264	−0.01598	0.088852	PC1	0.994194	−0.007177	−0.080523	−0.071012	0.080433
PC2	0.160308	−0.96524	0.205328	−0.0213	0.000975	PC2	0.010717	0.993644	−0.046254	0.102068	0.000834
PC3	−0.00192	0.208642	0.976229	−0.05866	0.000377	PC3	0.087246	0.035535	0.991102	0.094033	0.000278
PC4	0.01911	−0.00582	0.061247	0.997923	0.000114	PC4	−0.062061	0.106574	0.095359	−0.987774	0.000129
Talc											
Eigenvector	Band 1	Band 4	Band 8	Band 9	Eigenvalue	Eigenvector	Band 1	Band 4	Band 8	Band 9	Eigenvalue
PC1	0.981146	−0.08249	−0.17352	0.020952	0.077419	PC1	0.992041	−0.088076	−0.020357	−0.087656	0.077778
PC2	−0.11089	−0.98091	−0.15935	0.011179	0.002151	PC2	0.074608	0.927662	−0.365883	−0.00276	0.000987
PC3	−0.15727	0.175744	−0.97175	0.008834	0.000972	PC3	−0.060973	−0.359879	−0.924014	−0.113873	0.000668
PC4	−0.01793	0.011145	0.014006	0.999679	0.00012	PC4	0.081063	−0.046625	−0.109148	0.989617	0.000141
Calcite											
Eigenvector	Band 3	Band 4	Band 8	Band 9	Eigenvalue	Eigenvector	Band 3	Band 4	Band 8	Band 9	Eigenvalue
PC1	0.986451	0.034419	0.159074	0.020613	0.087008	PC1	0.995438	0.040073	−0.00247	−0.08655	0.089285
PC2	0.007967	−0.9866	0.16256	0.011646	0.003408	PC2	0.032823	−0.98973	−0.11559	−0.07745	0.00094
PC3	0.162753	−0.15922	−0.9737	−0.008666	0.000966	PC3	−0.00041	0.109912	−0.99115	0.074469	0.000804
PC4	−0.01902	0.009404	−0.01361	0.999682	0.00012	PC4	0.089585	−0.08215	0.065269	0.990437	0.000144
Dolomite											
Eigenvector	Band 1	Band 2	Band 4	Band 5	Eigenvalue	Eigenvector	Band 1	Band 2	Band 4	Band 5	Eigenvalue
PC1	0.986151	−0.13871	0.067819	−0.060554	0.088654	PC1	0.995477	−0.06488	−0.06847	−0.01132	0.069385
PC2	−0.1381	−0.98316	0.078174	0.09064	0.003984	PC2	−0.06967	−0.99261	−0.08169	0.056586	0.001457
PC3	−0.05614	0.087006	0.994625	0.000379	0.000461	PC3	0.062303	−0.0878	0.993768	−0.02886	0.000323
PC4	−0.07269	−0.08117	0.003376	−0.994041	0.000096	PC4	0.017047	0.053009	0.032599	0.997916	0.000061
Epidote											
Eigenvector	Band 1	Band 2	Band 5	Band 6	Eigenvalue	Eigenvector	Band 1	Band 2	Band 5	Band 6	Eigenvalue
PC1	−0.99463	0.077989	−0.01847	0.065481	0.078319	PC1	0.999321	−0.00051	−0.0121	−0.0348	0.061158
PC2	0.072129	0.993705	0.036176	−0.07771	0.003272	PC2	−0.00037	0.999147	0.024041	−0.03357	0.001385
PC3	−0.00765	−0.0207	0.982384	0.185567	0.000167	PC3	−0.01163	0.024486	−0.99955	0.013075	0.000114
PC4	0.073825	0.077714	−0.18241	0.977363	0.000095	PC4	−0.03496	−0.03324	−0.01347	−0.99875	0.000074

3.4. Spectral Angle Mapper

The spectral angle mapper (SAM) is a spectral supervised classification algorithm that assesses the spectral likeness between a pixel and the reference spectra in an n-dimensional space characterized by n spectral bands [3,51,53]. The reliability of the results of this algorithm depends on the training data (spectral library) and selected bands. It is calculated using the equation below:

$$\alpha = \cos^{-1} \left(\frac{\sum_{i=1}^{nb} t_i r_i}{\left(\sum_{i=1}^{nb} t_i^2 \right)^{\frac{1}{2}} \left(\sum_{i=1}^{nb} r_i^2 \right)^{\frac{1}{2}}} \right) \quad (2)$$

where “nb” represents the count of bands, “t” corresponds to a test spectrum, and “r” pertains to a reference spectrum. Employing this technique, the emphasis lies on the direction rather than the magnitude [51].

In this study, the spectral angle mapper (SAM) algorithm was employed through ENVI 5.3, utilizing an angle ranging between 0.1 and 0.2 radians to detect related mafic-ultramafic minerals. This method served as a supportive and complementary approach for other techniques while also effectively showcasing mafic-ultramafic minerals.

4. Results

4.1. FCC

This study examined various distinct FCCs on ASTER data with the aim of visualizing mafic-ultramafic complexes. Among these, FCCs 463 and 432 yielded the most effective results. As depicted in Figure 6, FCC 463, presented as an RGB composite, clearly revealed the ophiolitic complex through its light green coloring, encircled by a red boundary. The showcased ophiolitic complex is located to the southwest of Markazi Behsud, belonging to the Maidan Wardak province, and at the center of the Waras district, which is associated with the Bamyan province. These complexes primarily exhibit a trend in the NE-SW direction, aligning with the orientation of active faults in the vicinity. Furthermore, small ophiolite bodies are also discernible in various other areas, notably within the Panjab district.

Using RGB channels, the FCC 432 similarly delineated the ophiolitic complexes in these identical regions, denoting them with a deep green color (refer to Figure 7). The ophiolitic complex showcased within the red boundary maintains the same orientation as identified by FCC 463. These complexes are primarily distributed across the Markazi Behsud and Waras districts and might also extend toward the northeastern and western regions. Nevertheless, these extensions fall beyond the scope of our study area.

4.2. BR

Taking into consideration the spectral characteristics of ophiolitic complexes, along with their associated rocks and minerals, we conducted a comprehensive examination of both self-proposed and literature-based band ratios. Our focus was directed towards the identification of the spatial distribution of mafic-ultramafic rocks (such as dunite peridotite, and gabbro) and minerals (including carbonates, epidote, and chlorite). In the realm of band ratios, we delved into the utilization of various ratios. For the purpose of identifying mafic-ultramafic bodies, we explored the efficacy of the 12/14 band ratio as proposed by [3,61]. For the detection of dunite, the 4/3 ratio (a self-proposed band ratio) was employed due to the high reflectance of dunite in bands 4, while the 4/1 ratio, as described by [33,34], was found suitable for peridotite because it has maximum reflection in band 4 and low reflection in band 1 (Figure 4). Additionally, we introduced the 4/9 band ratio (self-proposed) to effectively identify gabbro rock bodies (as illustrated in Figure 8) due to the diagnostic characteristics of gabbro in bands 4 and 9, as shown in (Figure 4). The results obtained from these band ratios were combined and overlaid onto the hillshade representation of the area to enhance visualization and for better understanding, as depicted in Figure 8.

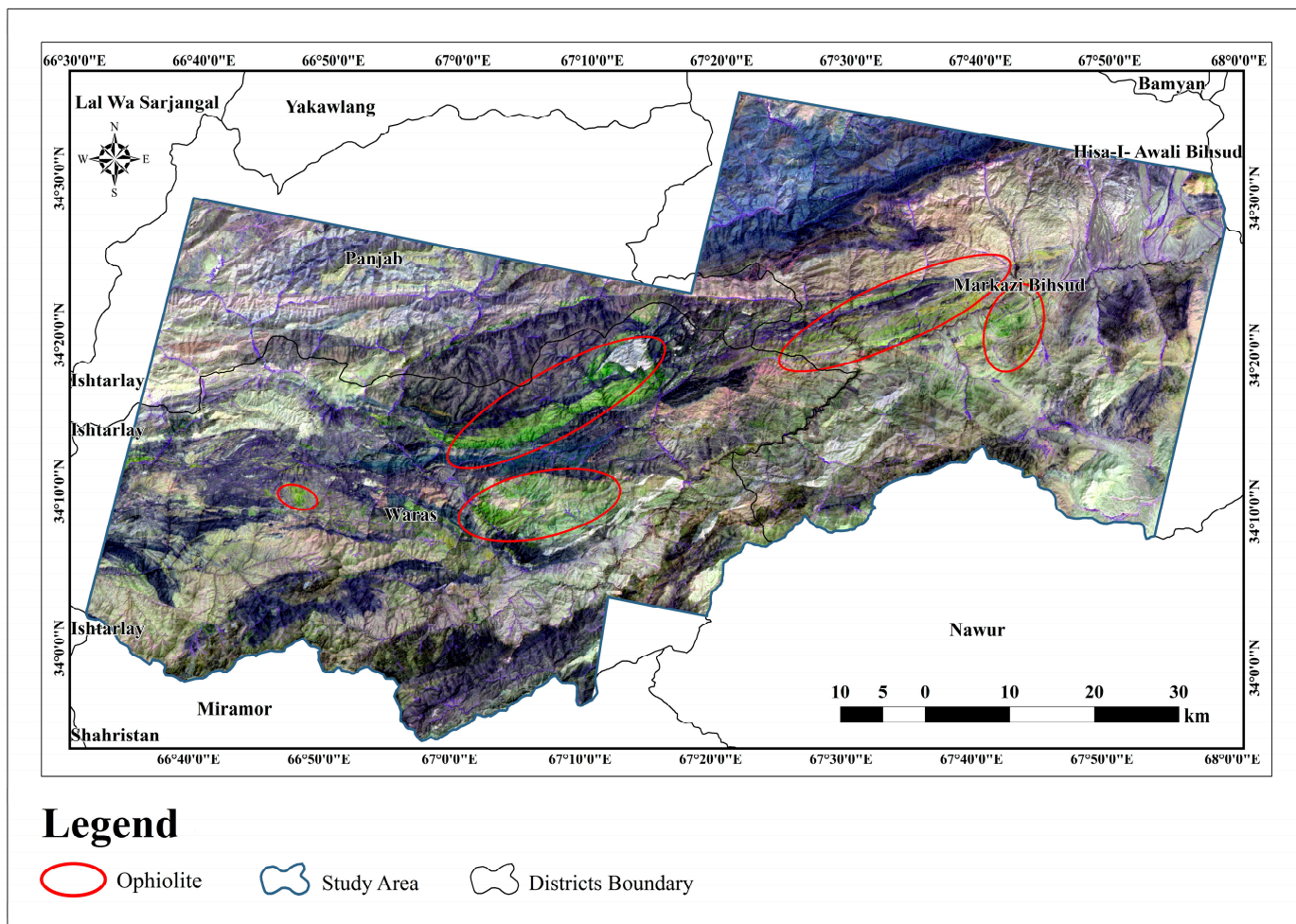


Figure 6. Visualization of the output generated from the 463-band combination presented as RGB channels using ASTER data.

The identified formations are in line with the outcomes of false color composites (FCCs), exhibiting a high degree of consistency. Notably, the distribution of mafic-ultramafic bodies spans across various sectors of this study area. Predominantly, dunite peridotites are prevalent in the northern and central sections of the Waras district, as well as extending across the western and central zones of the Markazi Behsud district (Figure 8). Additionally, smaller gabbroid rock formations are observable, coming into contact with dunite peridotites in the northeastern segments of the Waras district, as well as across the eastern and central parts of the Markazi Behsud district. The presence of peridotite bodies is also noted across these regions, with a notable concentration in the southern regions of the Panjab district (refer to Figure 8 for visualization).

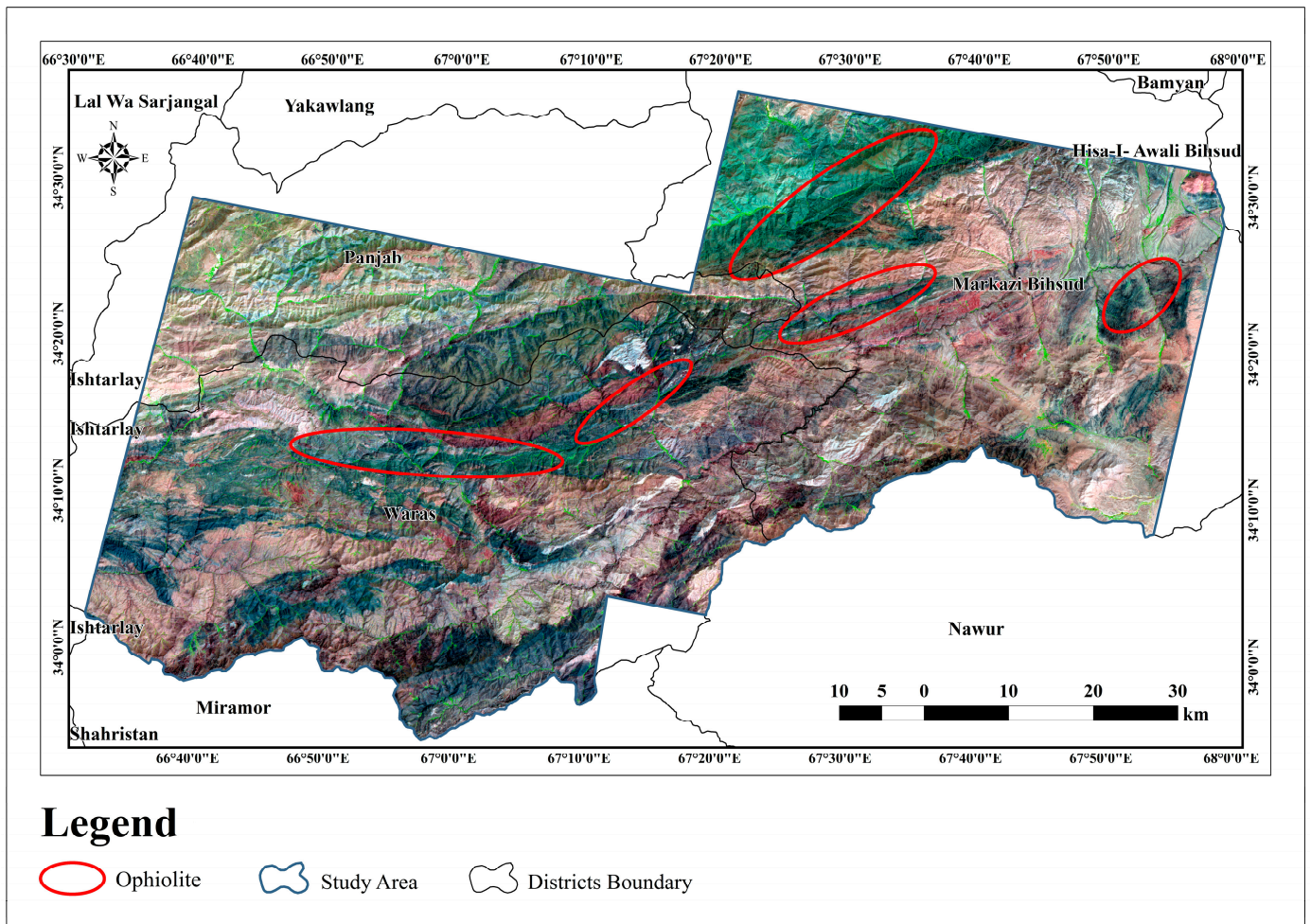


Figure 7. Visualization of the output generated from the 432-band combination presented as RGB channels using ASTER data.

Typically, mafic-ultramafic bodies are commonly followed by carbonate formations. To identify these carbonate minerals and other related mafic-ultramafic alteration minerals, we employed various band ratios. The band ratios 4/8, derived from the works of [3,16], were utilized to identify carbonate minerals. Additionally, a self-proposed ratio of 5/1 was applied for the epidote, and a 5/3 band ratio (also self-proposed) was employed for chlorite minerals. These ratios were assessed using ASTER data across this study area (refer to Figure 9). Presenting the results of each individual band ratio could potentially overwhelm readers with information, as it might make it challenging to highlight all the minerals within this study area. To address this, a comprehensive approach was taken: the outcomes from both the literature-based and self-proposed band ratios were amalgamated into a single map with different colors. This map was then superimposed with a hillshade representation of this study area, enhancing the visual clarity for readers' benefit (see Figure 9). As evident from (Figure 9), the spatial arrangement of epidote and chlorite aligns seamlessly with the identified ophiolitic complexes through alternative methods. Both minerals are distributed (NE-SW), which is corroborated by the FCC results. Their substantial presence is notably observed to the east of Markazi Behsud, as well as across the central and southern regions of the Waras districts. Furthermore, the geospatial distribution of carbonates is notably conspicuous to the west of Waras and in the southwest of Panjab districts. These areas directly interface with the ophiolitic complexes in the field (Figure 9).

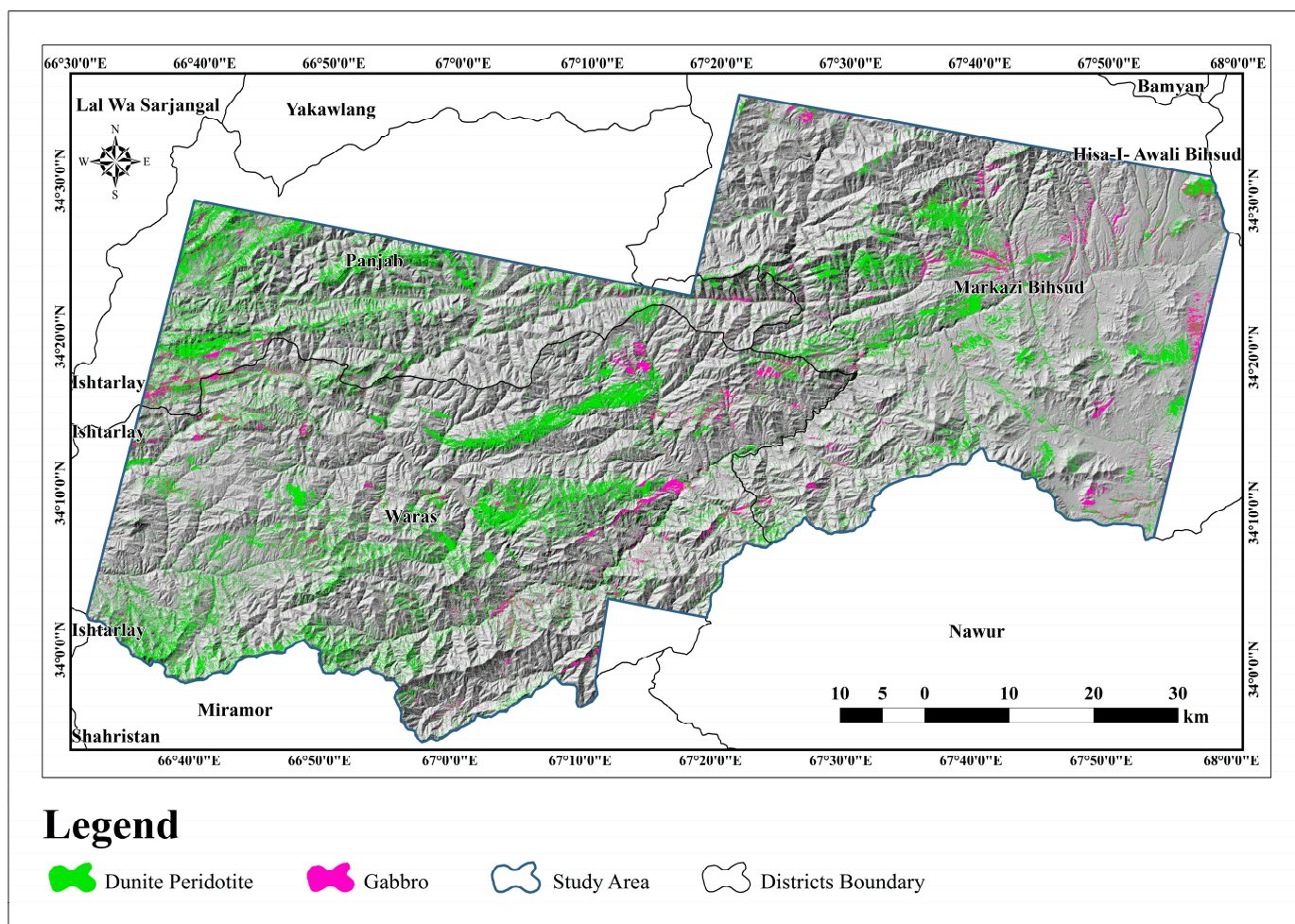


Figure 8. The combined results of diverse self-proposed and literature-based band ratios applied to the ASTER data over this study area identify the ophiolitic complex, showcasing the differentiation of mafic-ultramafic rocks across this study area.

4.3. PCA

The spectral transformation method, principal component analysis (PCA), was investigated in this study to distinguish mafic-ultramafic rocks (ophiolites) and their associated minerals. Various principal components (PCs) derived from rocks and minerals were analyzed, as outlined in Tables 4 and 5. Subsequently, the most informative PCs were chosen and utilized to generate thematic maps. Given the prevalence of mafic-ultramafic rocks in this study area and the potential for spectral overlap among similar rocks, a careful selection process was undertaken. The optimal component for representing peridotite, which characterizes ultramafics, was identified. Similarly, gabbro was chosen to represent mafic rocks, as detailed in Table 4 and illustrated in Figure 10.

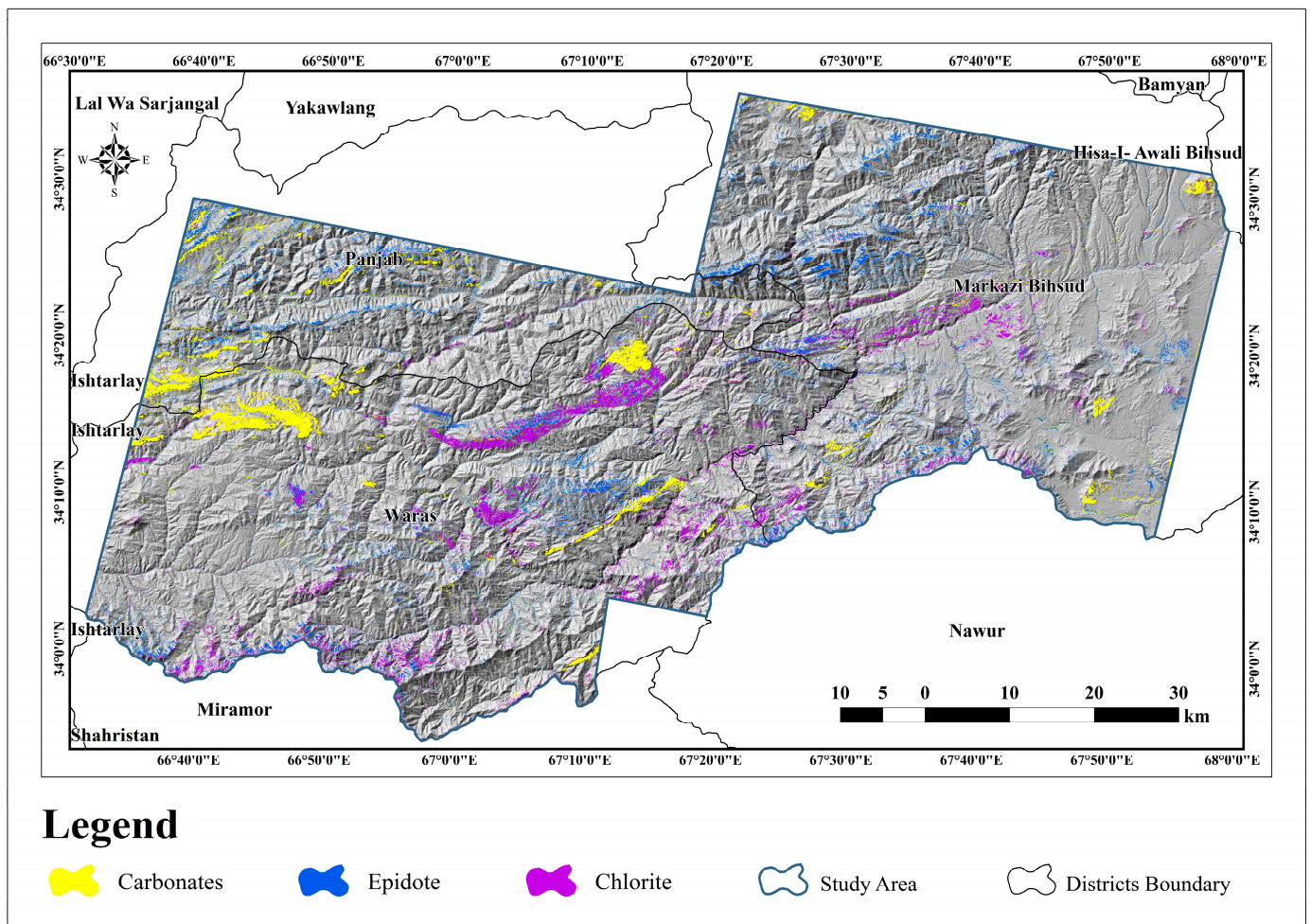


Figure 9. The spatial distribution of mafic-ultramafic minerals was identified using both self-proposed and literature-based band ratios on ASTER data.

The optimal principal components (PCs) for these rocks were determined by considering their maximum reflectance and absorption values. Among the bands evaluated, namely bands 1, 2, 4, and 6, an encouraging outcome emerged from the PCA analysis for peridotite. Conversely, for gabbro rocks, bands 2, 3, 7, and 8 demonstrated greater effectiveness, as outlined in Table 4.

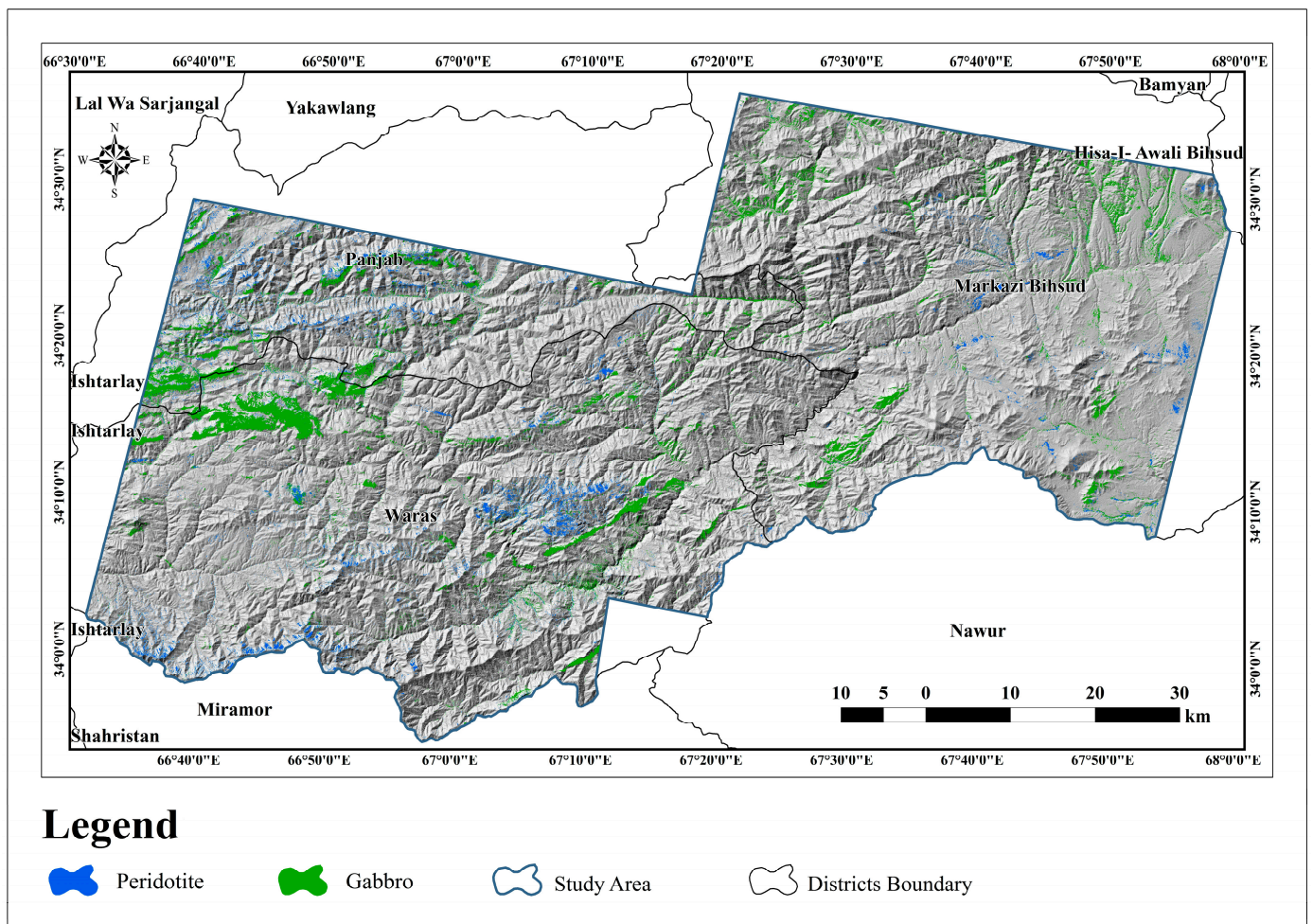


Figure 10. The distribution of peridotite and gabbro rocks was identified using the selected principal component statistical approach.

The distribution of mafic-ultramafic occurrences identified through the PCA approach aligns with the findings of other spectral analyses that were investigated. Moreover, PCA was also employed to identify carbonate minerals, talc, and chlorite, as delineated in Table 5. Bands 3, 4, 8, and 9 from ASTER data were thoughtfully selected for calcite identification, while bands 1, 4, 8, and 9 were chosen for talc, and bands 2, 3, 5, and 6 were specifically utilized for chlorite in the PCA analysis, as outlined in Table 5. As illustrated in Figure 11, this approach demonstrated its efficacy in identifying promising lithologies. The lithology was successfully pinpointed within regions characterized by the distribution of mafic-ultramafic rocks, underscoring the method's reliability. Notably, carbonates were detected in the northwestern portion of this study area, specifically within the Panjab district, where they exhibit clear associations with other mafic-ultramafic rocks.

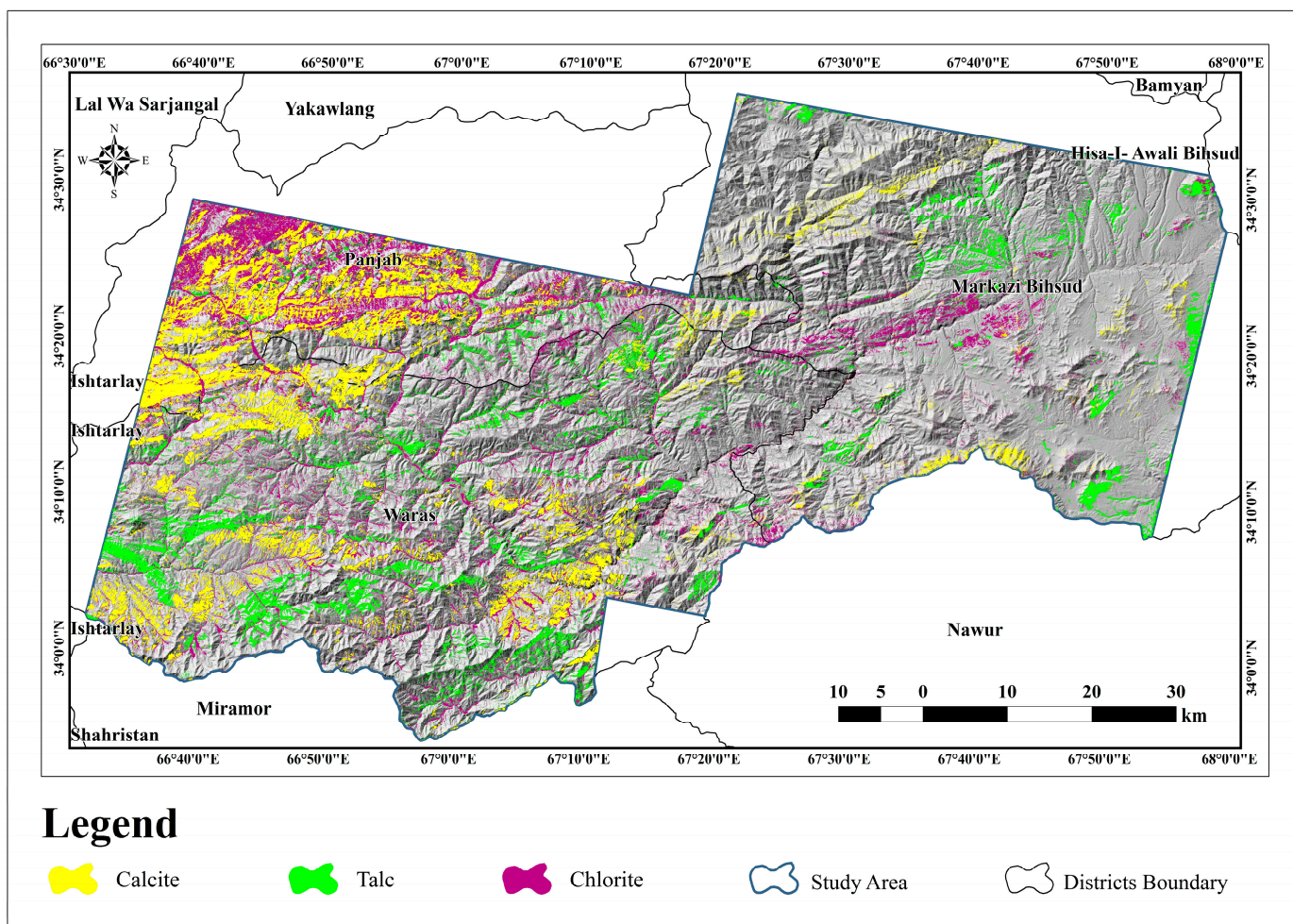


Figure 11. The distribution of calcite, talc, and chlorite minerals was identified through the selected principal components statistical approach.

4.4. SAM

In the realm of identifying mafic-ultramafic rocks and minerals, the utilization of supervised classification algorithms stands out. In this context, the effectiveness of the SAM was explored for the specific selection of rocks and minerals. For the establishment of reference or training data pertaining to rocks and minerals, two prominent spectral libraries were employed: the USGS spectral library and the Ecostress spectral library, developed by [64,65]. To represent the spectrum of mafic-ultramafic rocks, a comprehensive selection was made, including dunite peridotite, pyroxenite, serpentinite, and gabbro. Simultaneously, for the detection of mafic-ultramafic main and alteration minerals, notable choices such as carbonates, talc, and olivine were incorporated.

As illustrated in (Figure 12), the identification of specific rocks, notably peridotite and gabbro, can be observed across the Markazi Behsud and Waras districts. These identifications align coherently with the bodies detected using the FCC, BR, and PCA methods, substantiating the reliability of these techniques. Notably, in certain sections west of the Waras district, an amalgamation of mafic-ultramafic bodies is also discernible (Figure 12).

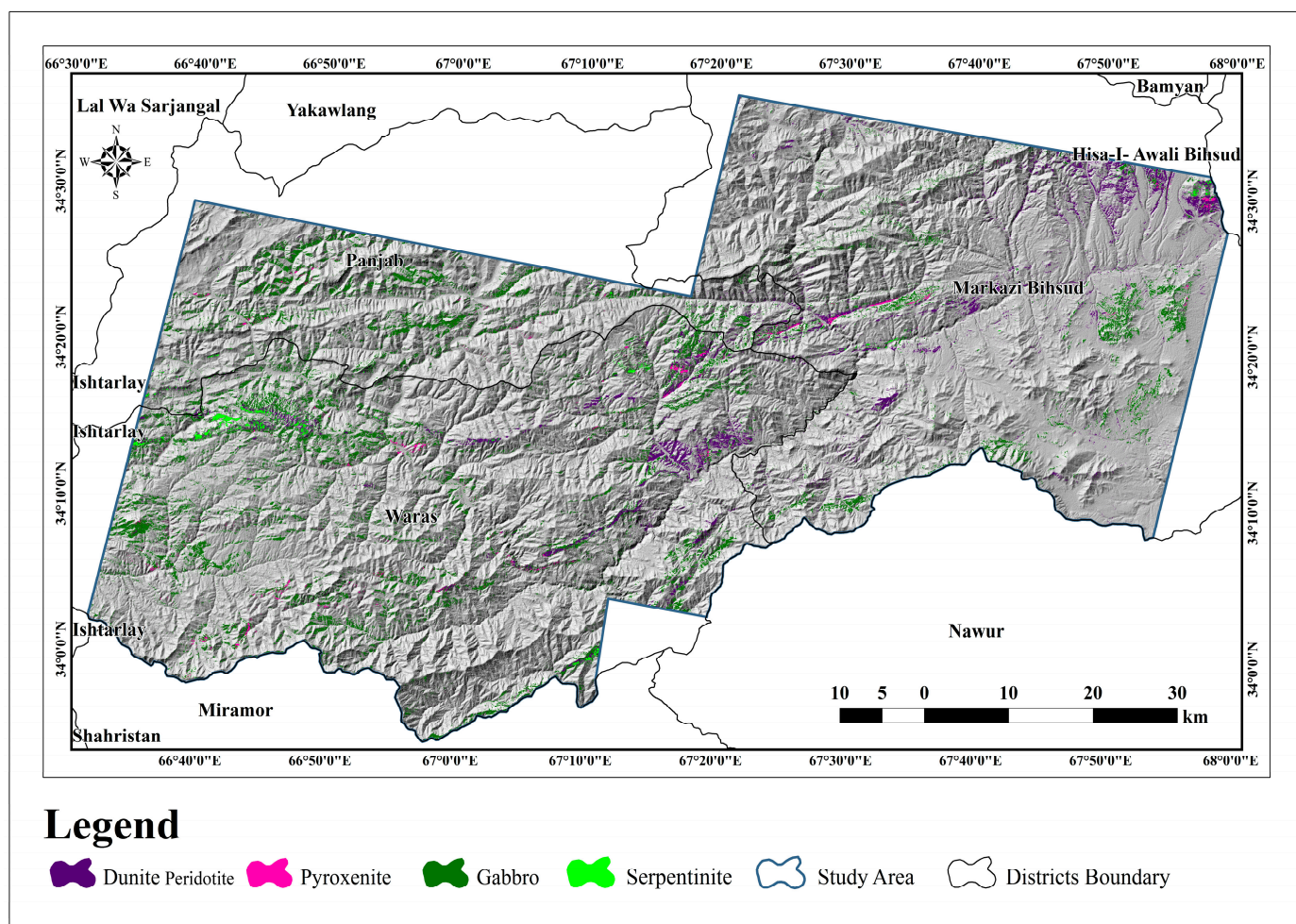


Figure 12. The spatial distribution of mafic-ultramafic rocks over this study area was detected by the SAM supervised classification algorithm in this study area.

Furthermore, SAM exhibited a remarkable capability in detecting pertinent mafic-ultramafic minerals, particularly carbonates and olivine. These minerals serve as indicative alteration minerals within the designated study area, as demonstrated in (Figure 13). Remarkably, the method effectively delineated the extent of carbonates, encompassing formations comprised of minute fragments of carbonate minerals.

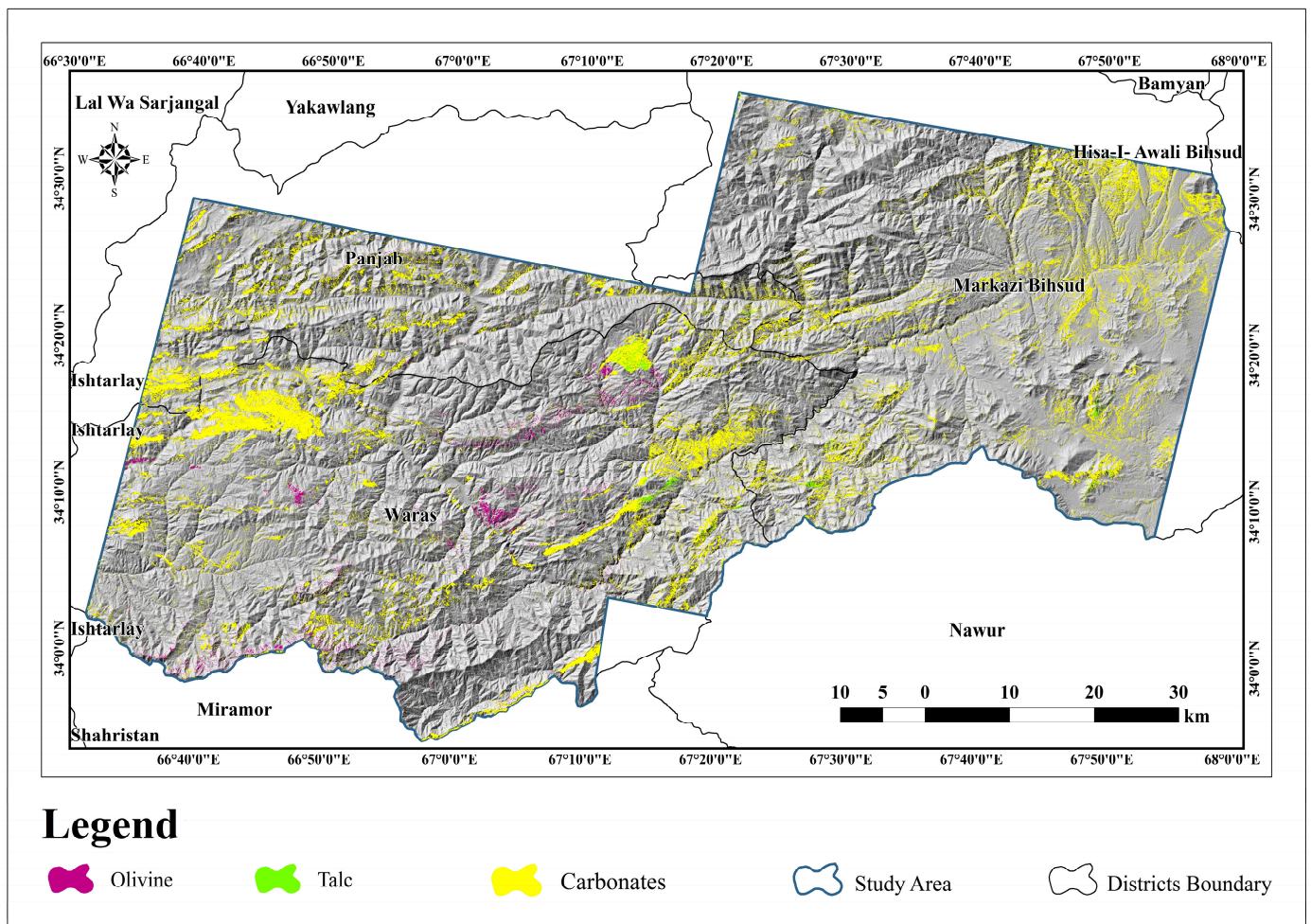


Figure 13. The spatial distribution of mafic-ultramafic minerals over this study area was detected by the SAM supervised classification algorithm in this study area.

The optimal outcomes attained through BR, PCA, and SAM have been consolidated into unified maps, enhancing the comprehension of the spatial distribution of Mesozoic ophiolitic complexes in central Afghanistan across the Maidan Wardak and Bamyan provinces. The most pertinent findings have been combined to highlight the spatial distribution of mafic-ultramafic rocks, also known as ophiolites (Figure 14). As depicted in the illustration, the distribution of ultramafic rocks appears to be sparse, surpassing the prevalence of mafic rocks within this study area. Consequently, this distribution delineates four distinct and promising regions of ophiolitic complexes. The first region, placing ophiolites, is situated to the northwest of the Markzi Behsud district, in correlation with Maidan Wardak province. This expanse spans approximately 40 km in length and 25 km in width, orienting itself in an NW-SE direction (refer to Figure 14).

The second area placing ophiolites is positioned on the southwestern expanse of the Markazi Behsud district, extending towards the central reaches of the Waras district, affiliated with Bamyan province. This auspicious ophiolite formation spans approximately 45 km in length and 7 km in width, positioned on the southern side of the Helmand fault zone (refer to Figure 14). Towards the northern periphery of the Helmand fault zone, the third region harboring ophiolites is positioned at the center of the Waras district, spanning an approximate length of 40 km and a width of 7 km. Both the second and third ophiolitic formations exhibit a NE-SW trend, aligning with the orientation of the Helmand fault zone (refer to Figure 14).

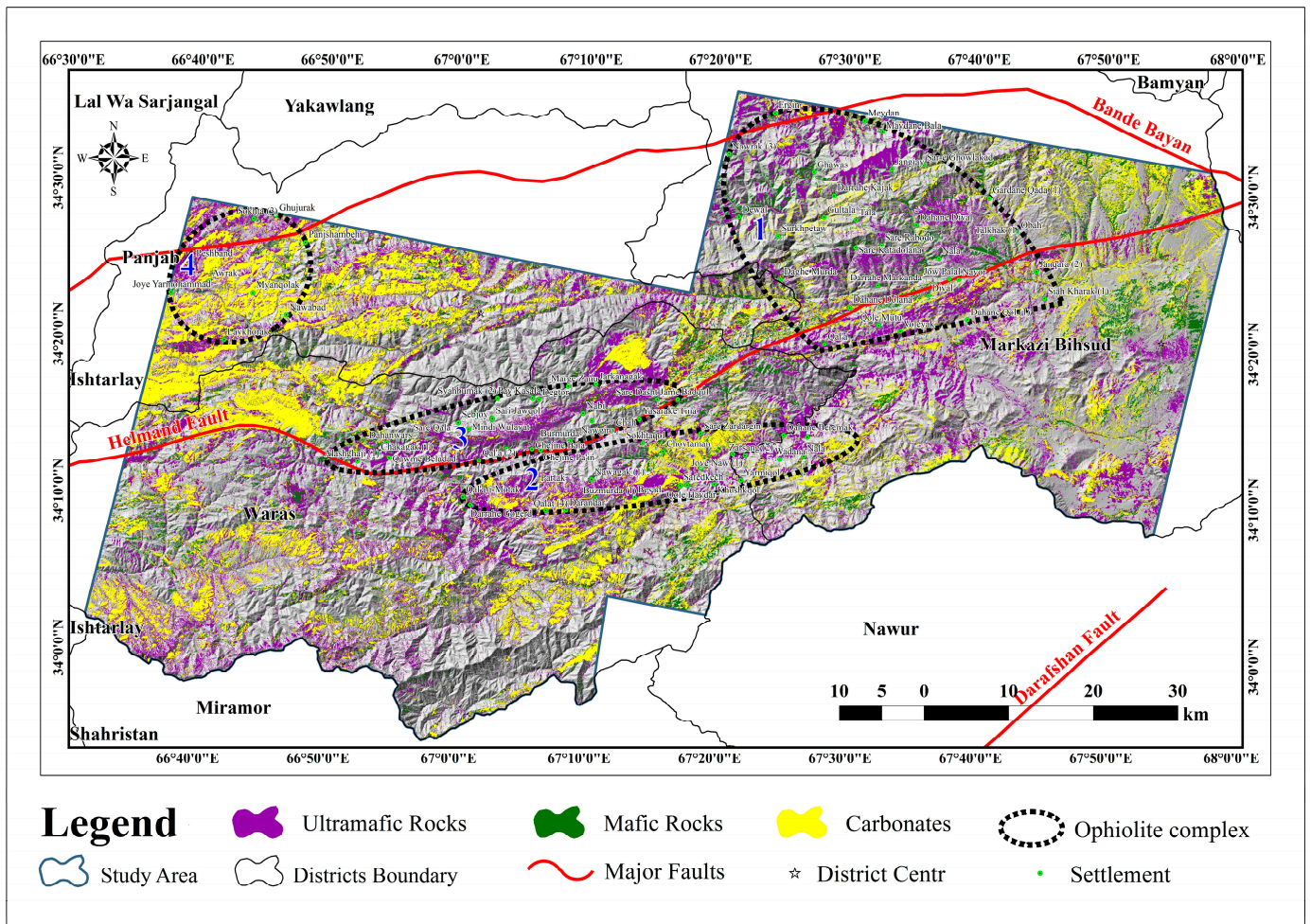


Figure 14. Spatial distribution of mafic-ultramafic rock formations (ophiolites) and carbonate formations identified through the utilization of BR, PCA, and SAM algorithms applied to ASTER data within this study area.

The fourth ophiolitic formation is located in the southwestern vicinity of the Panjab district, related to the Bamyan province along the Bande Bayan fault line. However, this particular body is unlikely to represent the primary mafic-ultramafic formation, as it predominantly comprises carbonate rocks and minerals. One can observe limited fragments of these rocks within this formation (refer to Figure 14).

As a result, the mafic-ultramafic minerals exhibit a widespread distribution across these four regions that contain ophiolites within this study area. This distribution has been obtained by integrating the most impactful outcomes from BR, PCA, and SAM methodologies (see Figure 15). Notably, the identified primary and altered minerals align with the extent and trend of the mafic-ultramafic rock formations, effectively affirming the efficacy of the employed algorithms.

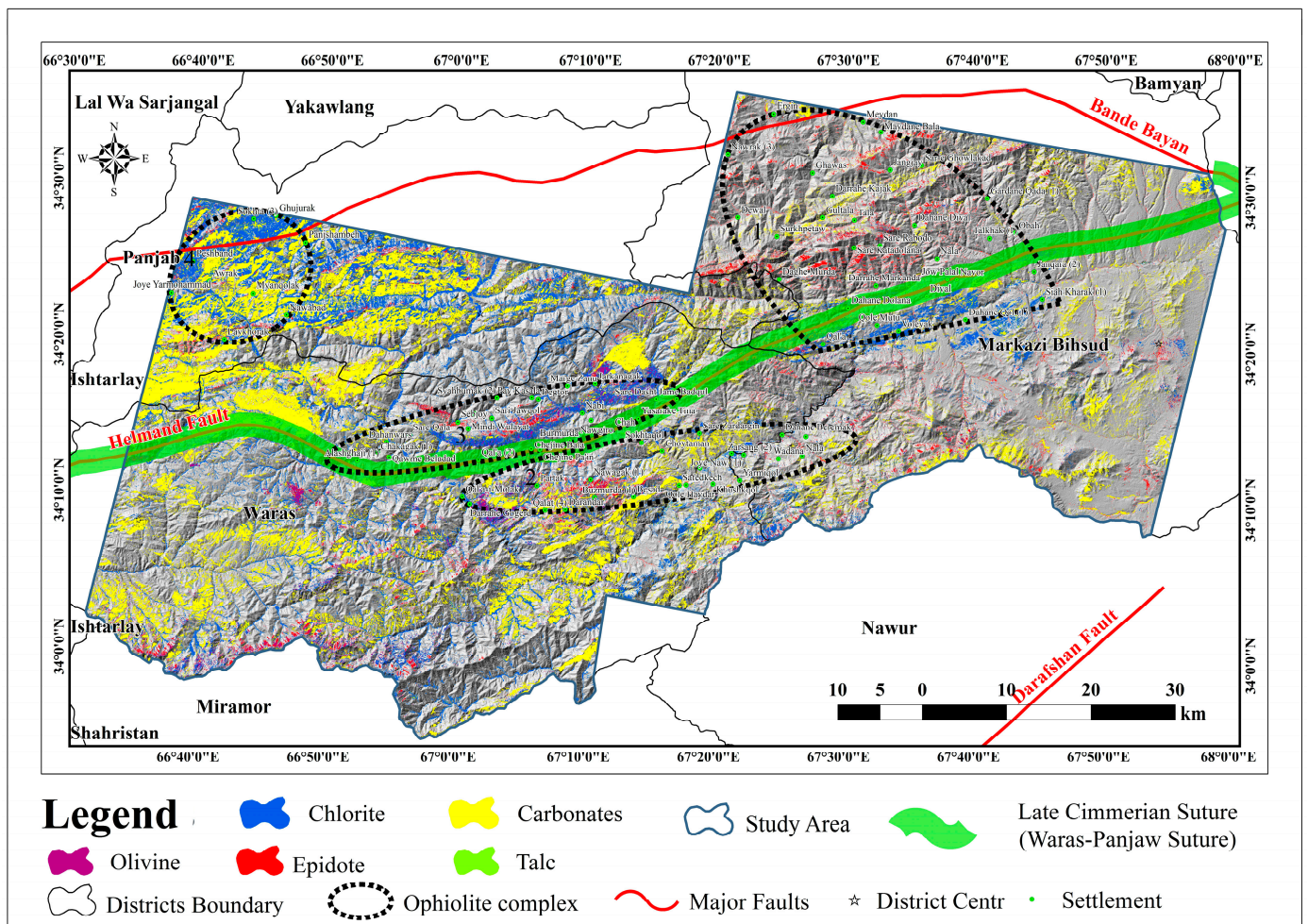


Figure 15. Spatial distribution of primary and altered mafic-ultramafic minerals derived using the BR, PCA, and SAM algorithms applied to ASTER data within this study area.

5. Discussion

The tectonic evolution of Afghanistan, which was shaped by the collision of Gondwanan and Eurasian fragments during the late Paleozoic era, has resulted in faults and suture zones that mark the boundaries of these fragments. These zones are characterized by the presence of ophiolite complexes, which are fragments of oceanic lithosphere that have been obducted (emplaced over continental crust) during collision events [7,64]. The identification of ophiolites has the potential to significantly improve our understanding of tectonic evolution and the history of past oceanic crust. In this study, we successfully detected four promising ophiolitic complexes in the central Afghanistan region, specifically in the Markazi Behsud district belonging to Maidan Wardak, Waras, and Panjab districts belonging to Bamyan. This was achieved using remote sensing data and a variety of analytical techniques, including false color composite (FCC), band ratio (BR), principal component analysis (PCA), and spectral angle mapper (SAM) (Figures 14 and 15). The identified ophiolitic complexes are located along the Helmand and Bande Bayan fault zones in central Afghanistan. Based on the ophiolitic classification of [7], these complexes are classified as Cimmerian ophiolites, which were formed during the Jurassic-Cretaceous period.

The suture zones, notably highlighted by [7,9], including locations such as Herat, Panjaw (Panjab), Kabul, and Khost, serve as crucial indicators of ophiolites and mélanges within Afghanistan’s geographical expanse. These suture zones, in conjunction with the identified ophiolites, offer valuable insights into the evolutionary trajectories of both paleo-Tethys and neo-Tethys in the region. This study represents the inaugural employment of

remote sensing techniques for ophiolite determination in central Afghanistan. While previous studies have traditionally employed conventional methods to map ophiolites as small entities, our research has successfully expanded the understanding of these formations. By identifying specific rock types and minerals (as illustrated in Figures 14 and 15), we have managed to extend the boundaries of these ophiolite bodies. In contrast to other ophiolite investigations, our study presents a substantial advancement in delineating ophiolite distribution across Afghanistan. Additionally, our methodology involving remote sensing data not only enriches ophiolite mapping practices but also contributes profoundly to the broader field.

The newly introduced band ratios presented in this study (Table 3) provide a valuable resource for mapping mafic-ultramafic rocks and minerals in arid and semi-arid regions. To validate the band ratios, a principal component analysis (PCA) was performed, which identified the same rock and mineral types. The convergence of the results from the different algorithms used in this study supports the efficacy of the proposed methodology. Ophiolites are composed of mafic and ultramafic rocks. In this study, we identified a variety of ultramafic rocks (e.g., dunite peridotite and pyroxenite) and mafic rocks (e.g., gabbro and basalt) in this study area, predominantly in the Markazi Behsud and Waras districts (Figure 14). Mafic rocks are often adjacent to ultramafic rocks. These rocks have often been altered, mainly to serpentine, during serpentinization. Therefore, we also identified key mafic-ultramafic minerals, including both primary and altered phases (e.g., calcite, chlorite, olivine, epidote, and talc) (Figure 15). This study area exhibits a notable prevalence of carbonates, concentrated in the southwestern region of the Panjab district. This indicates the potential alteration of mafic-ultramafic rocks, as supported by [2,65]. Carbonation of mafic-ultramafic rocks occurs in the presence of CO₂-rich fluids, which react with the abundant olivine and pyroxene in the rocks to form carbonates and hydrous silicates [2]. Carbonated ophiolites are thus evident throughout this study area, especially near the fourth identified body (Figure 14). Given that geological remote sensing methodologies are continuously developing, it becomes imperative that outcomes derived from remote sensing data and algorithms undergo validation through ground truth data. Within this study, a two-fold validation approach was employed. Firstly, the final results were cross-referenced against preexisting geological maps. Secondly, on-the-ground observations and sampling were carried out for verification purposes. Notably, a substantial alignment emerges between the ophiolite identifications made in our study and those documented in previous research and geological mapping endeavors.

During our field investigation, we meticulously collected control (test) points encompassing mafic, ultramafic, and carbonate rocks and minerals from various parts of this study area, as illustrated in Figure 16. In total, our efforts yielded 283 sample points representative of ultramafic rocks, 215 sample points for mafic rocks, and 150 sample points denoting carbonate rocks, all meticulously gathered during field observations. When subjected to accuracy assessment using a confusion matrix, it emerged that 209 out of 283 sample points for ultramafic rocks aligned with our results. For mafic rocks, 148 out of 215 sample points were consistent with our outcomes, while for carbonatic rocks, 111 out of the 150 collected sample points corresponded with our results. Calculating based on this matrix, an overall accuracy of 72.2% was attained, underscoring a commendable correlation between our derived findings and the field data.

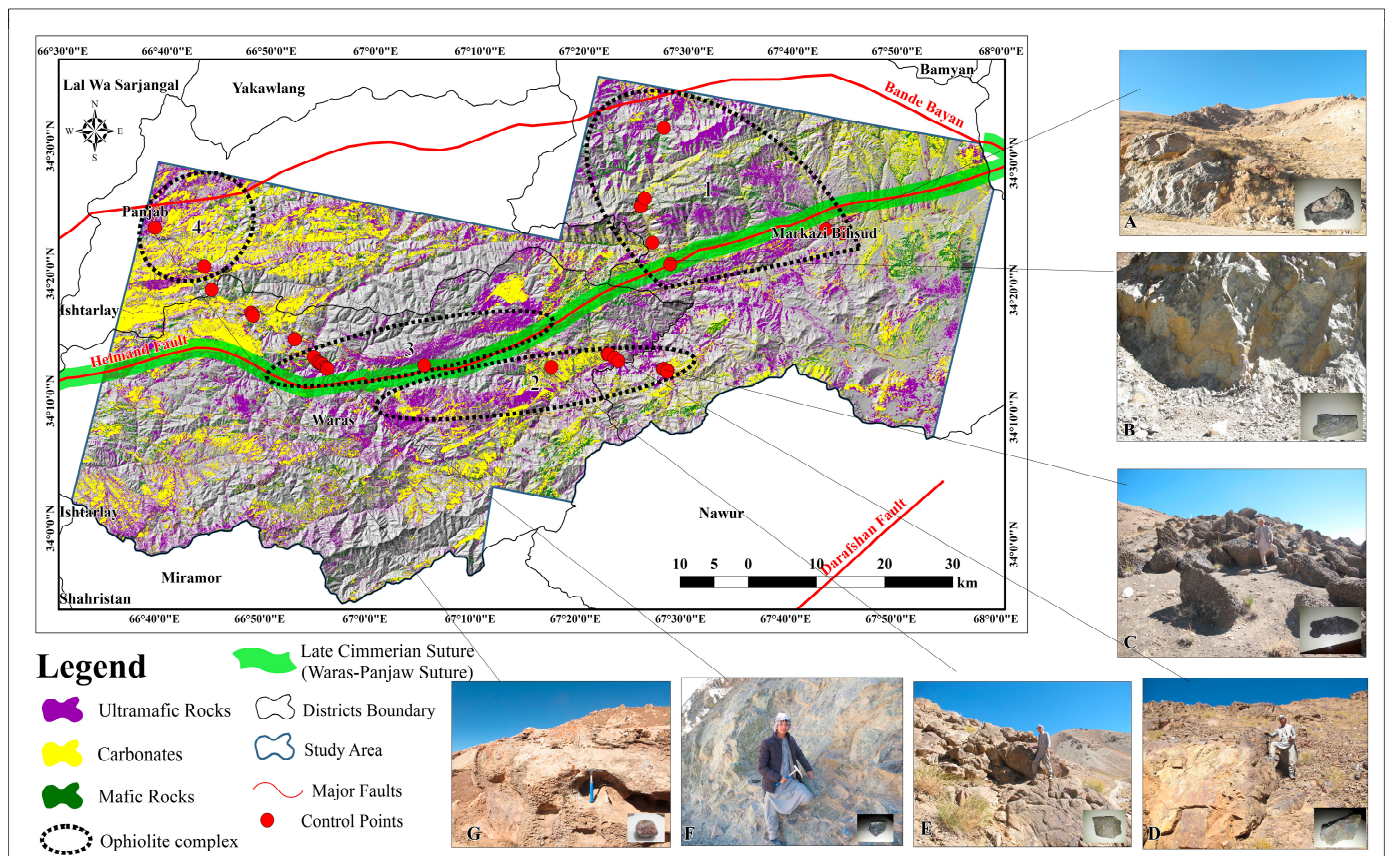


Figure 16. The final results depict the detected mafic-ultramafic rocks and the associated sampling strategy employed for validation purposes in this study area. The labeled components include: (A) Serpentinized ultramafic rocks; (B) Unaltered ultramafic rocks; (C) Unaltered mafic rocks; (D) Mafic rocks undergoing alteration; (E) Additional unaltered mafic rocks; (F) Composite of ultramafic rocks and serpentinite; and (G) Carbonate-rich rocks.

6. Conclusions

To achieve the primary objectives of this study, which were to delineate the Mesozoic ophiolitic complex in central Afghanistan using ASTER data and propose new band ratios for mapping these complexes, a variety of spectral analyses were employed, including false color composite (FCC), band ratio (BR), principal component analysis (PCA), and spectral angle mapper (SAM). These methodologies were applied across this study area to achieve the defined goal. Drawing upon the distinctive spectral features of mafic-ultramafic rocks and minerals in the Near-Infrared to Short-Wave Infrared (NIR-SWIR) spectrum, spectral libraries within the 0.50–2.50 μm wavelength range were consulted. Effective results were obtained through the application of two distinct band combinations: 463 and 432 in the RGB channels. These combinations proved highly effective in highlighting the ophiolitic complexes, thereby highlighting the mafic-ultramafic formations situated to the west of Markazi Behsud, as well as in the central Waras district.

A comprehensive examination of band ratios (BRs) was conducted, including both self-proposed and literature-based band ratios to detect ophiolite complexes. The BRs 12/14, 4/3, 4/1, and 4/9 were found to be effective in delineating and mapping mafic-ultramafic bodies, including dunite peridotite and gabbroic rocks, respectively. Additionally, the BRs 4/8, 5/1, and 5/3 were effective in identifying carbonates, epidote, and chlorite minerals. The identified mafic-ultramafic rocks and minerals aligned seamlessly with the visualized ophiolite complexes highlighted by the false color composite (FCC) imagery, sharing the same spatial orientation. To improve the accuracy and reliability of our results, we employed principal component analysis (PCA), a statistical method, to map mafic-ultramafic

formations (ophiolites) across this study area. In this study, we used PCA to analyze the spectral reflectance of this study area in the NIR-SWIR spectrum. Mafic-ultramafic rocks and minerals have distinctive spectral features in this range, which can be used to distinguish them from other rock types. By analyzing the maximum and minimum reflectance of these spectral features, we were able to identify mafic-ultramafic formations in this study area. The multispectral bands within the ASTER data proved to be instrumental in the spectral transformation process, facilitating the accurate delineation of ophiolitic formations. The outcomes derived from the PCA analysis served to reinforce the findings obtained through the application of False Color Composite (FCC) visualization and the self-proposed Band Ratios (BRs). Furthermore, as a part of this study, a supervised classification algorithm known as Spectral Angle Mapping (SAM) was also investigated. This analysis aimed to distinctly identify mafic-ultramafic rocks and minerals, encompassing elements like dunite, peridotite, pyroxenite, gabbro, serpentinite, olivine, talc, and carbonatic formations. The results derived from this examination aligned harmoniously with the outputs obtained from various other spectral analysis methodologies.

Ultimately, the gathered results were combined and merged to create a comprehensive thematic map that visually portrays the spatial distribution of mafic-ultramafic rocks (ophiolites) as well as the accompanying primary and alteration minerals. As a result, the culmination of these efforts led to the identification and delineation of four distinct regions enriched with ophiolitic formations across this study area. These notable ophiolitic-bearing regions encompass the northern sector of Markzi Behsud district within the Maidan Wardak province, the western region of Markzi Behsud, and the central expanse of the Waras district, affiliated with the Bamyan province. Additionally, these formations are conspicuously situated at the central locus of the Waras district, and an equally promising region graces the northwestern bounds of the Panjab district in Bamyan province.

The NW-SE and NE-SW trends of the ophiolitic complexes are consistent with the orientations of the Helmand and Bande Bayan fault zones, respectively. This suggests that the ophiolitic complexes were emplaced during the collision of tectonic plates along these fault zones.

The varying distributions of the ophiolitic complexes across this study area suggest that they have undergone different degrees of alteration. The unaltered ophiolitic complexes are likely to be younger and/or have been less exposed to weathering and hydrothermal fluids. The serpentine and carbonate formations are likely to be older and/or have been more exposed to weathering and hydrothermal fluids. The conclusive outcomes were subjected to thorough validation, involving cross-referencing with various geological and tectonic maps established in prior research endeavors. Additionally, a comprehensive dataset of 648 sample points was meticulously gathered, comprising 283 from ultramafic rocks, 215 from mafic rocks, and 150 from carbonate formations. These samples were meticulously collected during rigorous fieldwork conducted within this study area. The process of accuracy assessment yielded a remarkable result, indicating an overall accuracy rate of 72.2%. This level of precision signifies a substantial alignment between the delineated complexes on the map and the actual geological reality of this study area. This validation outcome underscores the reliability and quality of the mapping outcomes.

The findings of this study have significant implications for understanding the tectonic evolution and emplacement mechanisms of ophiolites during the Cimmerian orogenic events in the Paleo-Tethys context. The proposed techniques have the potential to be applied to other regions around the world, especially in arid and semi-arid environments, to map ophiolitic complexes and their constituent mafic-ultramafic rocks and minerals.

Author Contributions: Conceptualization, H.A. and M.R.H.; methodology, H.A. and M.R.H.; software, H.A., M.R.H. and A.Y.; validation, A.Y., A.B. (Alma Bekbotayeva), A.B. (Akmaral Baisalova) and E.P.; formal analysis, A.B.R., B.A. and I.M.; investigation, M.R.H. and A.Y.; resources, A.B. (Alma Bekbotayeva) and E.P.; data curation, I.M. and N.S.; writing—original draft preparation, H.A. and A.Y.; writing—review and editing, H.A. and M.R.H.; visualization, H.A. and M.R.H.; supervision, A.B.R. and E.P.; project administration, A.B. (Akmaral Baisalova), B.A. and I.M.; funding acquisition,

A.B. (Alma Bekbotayeva) and E.P. All authors have read and agreed to the published version of the manuscript.

Funding: This research received no external funding.

Data Availability Statement: Data are contained within the article.

Acknowledgments: The authors extend their gratitude to the anonymous reviewers and academic editor for their invaluable insights, constructive comments, and helpful suggestions, all of which significantly contributed to enhancing the quality of the manuscript. Additionally, we express our sincere appreciation to the NASA organization for generously providing the ASTER data, which greatly enriched the research.

Conflicts of Interest: The authors declare no conflict of interest.

References

1. Dilek, Y.; Furnes, H. Ophiolite genesis and global tectonics: Geochemical and tectonic fingerprinting of ancient oceanic lithosphere. *Bull. Geol. Soc. Am.* **2011**, *123*, 387–411. [\[CrossRef\]](#)
2. Yousufi, A.; Ahmadi, H.; Bekbotayeva, A.; Arshamov, Y.; Baisalova, A.; Omarova, G.; Pekkan, E. Integration of Remote Sensing and Field Data in Ophiolite Investigations: A Case Study of Logar Ophiolite Complex, SE Afghanistan. *Minerals* **2023**, *13*, 234. [\[CrossRef\]](#)
3. Ahmadi, H.; Kalkan, K. Mapping of Ophiolitic Complex in Logar and Surrounding Areas (SE Afghanistan) With ASTER Data. *J. Indian Soc. Remote Sens.* **2021**, *49*, 1271–1284. [\[CrossRef\]](#)
4. Condie, K.C.; Stern, R.J. Ophiolites: Identification and tectonic significance in space and time. *Geosci. Front.* **2023**, *14*, 101680. [\[CrossRef\]](#)
5. Kusky, T.M.; Windley, B.F.; Safonova, I.; Wakita, K.; Wakabayashi, J.; Polat, A.; Santosh, M. Recognition of ocean plate stratigraphy in accretionary orogens through Earth history: A record of 3.8 billion years of sea floor spreading, subduction, and accretion. *Gondwana Res.* **2013**, *24*, 501–547. [\[CrossRef\]](#)
6. Dilek, Y.; Furnes, H. Ophiolites and their origins. *Elements* **2014**, *10*, 93–100. [\[CrossRef\]](#)
7. Tapponnier, P.; Mattauer, M.; Proust, F.; Cassaigneau, C. Mesozoic ophiolites, sutures, and large-scale tectonic movements in Afghanistan. *Earth Planet. Sci. Lett.* **1981**, *52*, 355–371. [\[CrossRef\]](#)
8. Yousufi, A.; Bekbotayeva, A.; Muszynski, A.; Ahmadi, H.; Baibatsha, A. Distribution of ultramafic complexes in Afghanistan. *Int. Multidiscip. Sci. GeoConf. Surv. Geol. Min. Ecol. Manag. SGEM* **2019**, *19*, 163–170.
9. Siehl, A. Structural setting and evolution of the Afghan orogenic segment—A review. *Geol. Soc. Spec. Publ.* **2017**, *427*, 57–88. [\[CrossRef\]](#)
10. Benham, A.J.; Kováč, P.; Petterson, M.G.; Rojkovic, I.; Styles, M.T.; Gunn, A.G.; Mckerverey, J.A.; Wasy, A. Chromite and PGE in the logar ophiolite complex, Afghanistan. *Trans. Inst. Min. Metall. Sect. B Appl. Earth Sci.* **2009**, *118*, 45–58. [\[CrossRef\]](#)
11. Belgrano, T.M.; Diamond, L.W.; Novakovic, N.; Hewson, R.D.; Hecker, C.A.; Wolf, R.C.; de Doliwa Zielinski, L.; Kuhn, R.; Gilgen, S.A. Multispectral discrimination of spectrally similar hydrothermal minerals in mafic crust: A 5000 km² ASTER alteration map of the Oman–UAE ophiolite. *Remote Sens. Environ.* **2022**, *280*, 113211. [\[CrossRef\]](#)
12. Bamoussa, A.O.; Matar, S.S.; Daoudi, M. Detecting and Distinguishing Ophiolite Rocks via Multispectral Remote Sensing in Bi'r Umq, Southeast Al Madinah Al Munawwarah, Saudi Arabia. *Int. J. Geosci.* **2021**, *12*, 635–652. [\[CrossRef\]](#)
13. Qasim, M.; Khan, S.D.; Haider, R.; Rasheed, M.U. Integration of multispectral and hyperspectral remote sensing data for lithological mapping in Zhob Ophiolite, Western Pakistan. *Arab. J. Geosci.* **2022**, *15*, 599. [\[CrossRef\]](#)
14. Mohan, M.; Meyyappan, M. Mapping of mafic-ultramafic rocks in SMUC-SGT, India using ASTER & Sentinel-2A satellite images. *Remote Sens. Appl. Soc. Environ.* **2022**, *28*, 100826. [\[CrossRef\]](#)
15. Eskandari, A.; Hosseini, M.; Nicotra, E. Application of Satellite Remote Sensing, UAV-Geological Mapping, and Machine Learning Methods in the Exploration of Podiform Chromite Deposits. *Minerals* **2023**, *13*, 251. [\[CrossRef\]](#)
16. Çörtük, R.M.; Çelik, Ö.F.; Alkan, A.; Özkan, M.; Özyavaş, A. Distribution of rocks in Pınarbaşı Ophiolite from central Anatolia (Turkey) based on analysis of ASTER and Landsat-8 data. *Geol. J.* **2020**, *55*, 6810–6822. [\[CrossRef\]](#)
17. Khedr, M.Z.; Kamh, S.; Al Desouky, A.A.; Takazawa, E.; Hauzenberger, C.; Whattam, S.A.; El-Awady, A. Remote sensing and geochemical investigations of sulfide-bearing metavolcanic and gabbroic rocks (Egypt): Constraints on host-rock petrogenesis and sulfide genesis. *Gondwana Res.* **2023**, *119*, 282–312. [\[CrossRef\]](#)
18. Eldougdoug, A.; Abdelazeem, M.; Gobashy, M.; Abdelwahed, M.; Abd El-Rahman, Y.; Abdelhalim, A.; Said, S. Exploring gold mineralization in altered ultramafic rocks in south Abu Marawat, Eastern Desert, Egypt. *Sci. Rep.* **2023**, *13*, 7293. [\[CrossRef\]](#)
19. Lasheen, E.S.R.; Mohamed, W.H.; Elyaseer, M.H.; Rashwan, M.A.; Azer, M.K. Geochemical and remote sensing integrated with satellite gravity data of Darhib and Atshan talc deposits, South Eastern Desert, Egypt. *Sci. Rep.* **2023**, *13*, 9108. [\[CrossRef\]](#)
20. Lukose, L.; Dutta, D.; Rajkakati, M.; Guha, A.; Bhowmik, S.K. The reflectance spectroscopy of ultramafic rocks from the Nagaland Ophiolite Complex, NE India: Convergence of spectroscopic and petrological analyses. *J. Earth Syst. Sci.* **2023**, *132*, 96. [\[CrossRef\]](#)

21. Pinet, P.C.; Ceuleneer, G. Hyperspectral Survey for Mantle Rock Surface Mineralogy Mapping of the Sumail/Maqsad Peridotitic Massif. In Proceedings of the International Conference on Ophiolites and the Oceanic Lithosphere: Results of the Oman Drilling Project and Related Research, Muscat, Oman, 12–14 January 2020; Sultan Qaboos University: Seeb, Oman, 2020; pp. 190–192.
22. Libeesh, N.K.; Arivazhagan, S. Spectral pathways for effective delineation of mafic-ultramafic rocks by using PRISMA hyperspectral data. *Remote Sens. Appl. Soc. Environ.* **2023**, *30*, 100955. [[CrossRef](#)]
23. Ninomiya, Y.; Fu, B.; Cudahy, T.J. Detecting lithology with Advanced Spaceborne Thermal Emission and Reflection Radiometer (ASTER) multispectral thermal infrared “radiance-at-sensor” data. *Remote Sens. Environ.* **2005**, *99*, 127–139. [[CrossRef](#)]
24. Guha, A.; Vinod Kumar, K. New ASTER derived thermal indices to delineate mineralogy of different granitoids of an Archaean Craton and analysis of their potentials with reference to Ninomiya’s indices for delineating quartz and mafic minerals of granitoids—An analysis in Dharwar Cr. *Ore Geol. Rev.* **2016**, *74*, 76–87. [[CrossRef](#)]
25. Madani, A.; Harbi, H. Utilization of Remote Sensing Techniques For Mapping The Listwaenite Associated With Jabalal-Wask Ophiolite Complex, Northwestern Saudi Arabia. *Egypt. J. Remote Sens. Space Sci.* **2008**, *11*, 57–72.
26. Abdelmalik, K.W.; Abd-Allah, A.M.A. Integration of remote sensing technique and field data in geologic mapping of an ophiolitic suture zone in western Arabian Shield. *J. Afr. Earth Sci.* **2018**, *146*, 180–190. [[CrossRef](#)]
27. Mehdikhani, B.; Imamalipour, A. ASTER-based remote sensing image analysis for prospection criteria of podiform chromite at the khoy ophiolite (NW Iran). *Minerals* **2021**, *11*, 960. [[CrossRef](#)]
28. Gürsoy, Ö. Hybrid Band Combination for Discriminating Lithology of Dunite in Ultramafic Rocks. *J. Indian Soc. Remote Sens.* **2019**, *47*, 1041–1049. [[CrossRef](#)]
29. Tangestani, M.H.; Jaffari, L.; Vincent, R.K.; Sridhar, B.B.M. Spectral characterization and ASTER-based lithological mapping of an ophiolite complex: A case study from Neyriz ophiolite, SW Iran. *Remote Sens. Environ.* **2011**, *115*, 2243–2254. [[CrossRef](#)]
30. Rajendran, S.; Nasir, S. Mapping of Moho and Moho Transition Zone (MTZ) in Samail ophiolites of Sultanate of Oman using remote sensing technique. *Tectonophysics* **2015**, *657*, 63–80. [[CrossRef](#)]
31. Khan, S.D.; Mahmood, K.; Casey, J.F. Mapping of Muslim Bagh ophiolite complex (Pakistan) using new remote sensing, and field data. *J. Asian Earth Sci.* **2007**, *30*, 333–343. [[CrossRef](#)]
32. Othman, A.A.; Gloaguen, R. Improving lithological mapping by SVM classification of spectral and morphological features: The discovery of a new chromite body in the Mawat ophiolite complex (Kurdistan, NE Iraq). *Remote Sens.* **2014**, *6*, 6867–6896. [[CrossRef](#)]
33. Eslami, A.; Ghaderi, M.; Rajendran, S.; Pour, A.B.; Hashim, M. Integration of ASTER and landsat TM remote sensing data for chromite prospecting and lithological mapping in Neyriz ophiolite zone, south Iran. *Resour. Geol.* **2015**, *65*, 375–388. [[CrossRef](#)]
34. Pournamdari, M.; Hashim, M.; Pour, A.B. Application of ASTER and Landsat TM data for geological mapping of esfandagheh ophiolite complex, southern Iran. *Resour. Geol.* **2014**, *64*, 233–246. [[CrossRef](#)]
35. Ghoneim, S.M.; Yehia, M.A.; Salem, S.M.; Ali, H.F. Integrating remote sensing data, GIS analysis and field studies for mapping alteration zones at Wadi Saqia area, central Eastern Desert, Egypt. *Egypt. J. Remote Sens. Space Sci.* **2022**, *25*, 323–336. [[CrossRef](#)]
36. Bosquez, S.; Alferez, G.H.; Ardila, A.M.M.; Clausen, B.L. Automatic Classification of Felsic, Mafic, and Ultramafic Rocks in Satellite Images from Palmira and La Victoria, Colombia. In Proceedings of the Lecture Notes in Networks and Systems; Springer Science and Business Media Deutschland GmbH, Online, 14–15 July 2022; Volume 507 LNNS, pp. 531–547.
37. Shebl, A.; Hamdy, M. Multiscale (microscopic to remote sensing) preliminary exploration of auriferous-uraniferous marbles: A case study from the Egyptian Nubian Shield. *Sci. Rep.* **2023**, *13*, 9173. [[CrossRef](#)] [[PubMed](#)]
38. Manap, H.S.; San, B.T. Data Integration for Lithological Mapping Using Machine Learning Algorithms. *Earth Sci. Inform.* **2022**, *15*, 1841–1859. [[CrossRef](#)]
39. Shirmard, H.; Farahbakhsh, E.; Müller, R.D.; Chandra, R. A review of machine learning in processing remote sensing data for mineral exploration. *Remote Sens. Environ.* **2022**, *268*, 112750. [[CrossRef](#)]
40. Abdelaziz, R.; Abd El-Rahman, Y.; Wilhelm, S. Landsat-8 data for chromite prospecting in the Logar Massif, Afghanistan. *Heliyon* **2018**, *4*, e00542. [[CrossRef](#)]
41. Abdullah, S.H.; Chmyriov, V.M.; Dronov, V.I. *Geology and Mineral Resources of Afghanistan*; British Geological Survey: Nottingham, UK, 2008; Volume 2.
42. Boulín, J. Hercynian and Eocimmerian events in Afghanistan and adjoining regions. *Tectonophysics* **1988**, *148*, 253–278. [[CrossRef](#)]
43. Shroder, J.F.; Eqrar, N.; Waizy, H.; Ahmadi, H.; Weihs, B.J. Review of the Geology of Afghanistan and its water resources. *Int. Geol. Rev.* **2021**, *64*, 1009–1031. [[CrossRef](#)]
44. Boulín, J. Afghanistan structure, greater India concept and Eastern Tethys evolution. *Tectonophysics* **1981**, *72*, 261–287. [[CrossRef](#)]
45. Termier, H.; Termier, G. Position entre Gondwana et Téthys des provinces afghanes au Carbonifère et au Permien. Essai biogéographique. *Mémoires Hors Série la Société Géologique Fr.* **1977**, *8*, 309–324.
46. Blaise, J.; Bordet, P.; Carbonnel, J.P.; Montenat, C. Flyschs et ophiolites dans la region de Panjaw; une suture neocimmerienne en Afghanistan central. *Bull. la Société Géologique Fr.* **1978**, *S7-XX*, 795–798. [[CrossRef](#)]
47. Boulín, J. Neocimmerian events in Central and Western Afghanistan. *Tectonophysics* **1990**, *175*, 285–315. [[CrossRef](#)]
48. Wheeler, B.L.; Bufe, C.G.; Johnson, M.L. *Seismotectonic Map of Afghanistan, with Annotated Bibliography*; U.S. Geological Survey Open-File Report; U.S. Geological Survey: Reston, VA, USA, 2005.

49. Ruleman, C.A.; Crone, A.J.; Machette, M.N.; Haller, K.M.; Rukstales, K.S. *Map and Database of Probable and Possible Quaternary Faults in Afghanistan*; USGS Afghanistan Project Product No. 150, Open-File Rep. 2007-1103; U.S. Geological Survey: Reston, VA, USA, 2007.
50. Ahmadi, H.; Pekkan, E.; Seyitoğlu, G. Automatic lineaments detection using radar and optical data with an emphasis on geologic and tectonic implications: A case study of Kabul block, Southeast Afghanistan. *Geocarto Int.* **2023**, *38*, 2231400. [[CrossRef](#)]
51. Mashkoo, R.; Ahmadi, H.; Rahmani, A.B.; Pekkan, E. Detecting Li-Bearing Pegmatites Using Geospatial Technology: The Case of SW Konar Province, Eastern Afghanistan. *Geocarto Int.* **2022**, *37*, 14105–14126. [[CrossRef](#)]
52. NASA ASTER | Terra. Available online: <https://terra.nasa.gov/about/terra-instruments/aster> (accessed on 7 April 2022).
53. Ahmadi, H.; Uygucgil, H. Targeting iron prospective within the Kabul Block (SE Afghanistan) via hydrothermal alteration mapping using remote sensing techniques. *Arab. J. Geosci.* **2021**, *14*, 183. [[CrossRef](#)]
54. Aboelkhair, H.; Abdelhalim, A.; Hamimi, Z.; Al-Gabali, M. Reliability of using ASTER data in lithologic mapping and alteration mineral detection of the basement complex of West Berenice, Southeastern Desert, Egypt. *Arab. J. Geosci.* **2020**, *13*, 287. [[CrossRef](#)]
55. Shebl, A.; Abdellatif, M.; Elkhateeb, S.O.; Csámer, Á. Multisource Data Analysis for Gold Potentiality Mapping of Atalla Area and Its Environs, Central Eastern Desert, Egypt. *Minerals* **2021**, *11*, 641. [[CrossRef](#)]
56. Jensen, J.R. *Introductory Digital Image Processing: A Remote Sensing Perspective*, 4th ed.; Pearson Publication: London, UK, 2015; ISBN 0132058405.
57. Pour, A.B.; Hashim, M.; Hong, J.K.; Park, Y. Lithological and alteration mineral mapping in poorly exposed lithologies using Landsat-8 and ASTER satellite data: North-eastern Graham Land, Antarctic Peninsula. *Ore Geol. Rev.* **2019**, *108*, 112–133. [[CrossRef](#)]
58. Beiranvand Pour, A.; Hashim, M.; Pournamdari, M. Chromitite Prospecting Using Landsat TM and Aster Remote Sensing Data. *ISPRS Ann. Photogramm. Remote Sens. Spat. Inf. Sci.* **2015**, *2*, 99–103. [[CrossRef](#)]
59. Ge, W.; Cheng, Q.; Jing, L.; Armenakis, C.; Ding, H. Lithological discrimination using ASTER and Sentinel-2A in the Shibanzing ophiolite complex of Beishan orogenic in Inner Mongolia, China. *Adv. Space Res.* **2018**, *62*, 1702–1716. [[CrossRef](#)]
60. Cardoso-Fernandes, J.; Teodoro, A.C.; Lima, A. Remote sensing data in lithium (Li) exploration: A new approach for the detection of Li-bearing pegmatites. *Int. J. Appl. Earth Obs. Geoinf.* **2019**, *76*, 10–25. [[CrossRef](#)]
61. Emam, A.; Zoheir, B.; Johnson, P. ASTER-based mapping of ophiolitic rocks: Examples from the Allaqi-Heiani suture, SE Egypt. *Int. Geol. Rev.* **2016**, *58*, 525–539. [[CrossRef](#)]
62. Meerdink, S.K.; Hook, S.J.; Roberts, D.A.; Abbott, E.A. The ECOSTRESS spectral library version 1.0. *Remote Sens. Environ.* **2019**, *230*, 111196. [[CrossRef](#)]
63. Elaaraj, A.; Lhachmi, A.; Tabyaoui, H.; Alitane, A.; Varasano, A.; Hitouri, S.; El Yousfi, Y.; Mohajane, M.; Essahlaoui, N.; Gueddari, H.; et al. Remote Sensing Data for Geological Mapping in the Saka Region in Northeast Morocco: An Integrated Approach. *Sustainability* **2022**, *14*, 15349. [[CrossRef](#)]
64. Brunn, J.H.J.; Dumont, J.F.; De Graciansky, P.C.; Gutnic, M.; Juteau, T.; Marcoux, J.; Monod, O.; Poisson, A. Outline of the geology of the western Taurids. *Geol. Hist. Turk.* **1971**, *13*, 225–255.
65. Boskabadi, A.; Pitcairn, I.K.; Broman, C.; Boyce, A.; Teagle, D.A.H.; Cooper, M.J.; Azer, M.K.; Stern, R.J.; Mohamed, F.H.; Majka, J. Carbonate alteration of ophiolitic rocks in the Arabian–Nubian Shield of Egypt: Sources and compositions of the carbonating fluid and implications for the formation of Au deposits. *Int. Geol. Rev.* **2017**, *59*, 391–419. [[CrossRef](#)]

Disclaimer/Publisher’s Note: The statements, opinions and data contained in all publications are solely those of the individual author(s) and contributor(s) and not of MDPI and/or the editor(s). MDPI and/or the editor(s) disclaim responsibility for any injury to people or property resulting from any ideas, methods, instructions or products referred to in the content.